Modelling the in-plane strain rate dependent behaviour of woven composites with special emphasis on the non-linear shear response

Modelling the in-plane strain rate dependent behaviour of woven composites with special emphasis on the non-linear shear response

F. Martínez-Hergueta[1*], D. Ares[2], A. Ridruejo[2], J. Wiegand[3], N. Petrinic[4]

[1] *School of Engineering, Institute for Infrastructure and Environment, University of Edinburgh, William Rankine Building, Edinburgh, EH9 3FG, UK.*

[2] *Department of Materials Science, Technical University of Madrid, E. T. S. de Ingenieros de Caminos. Madrid, 28040, Spain*

[3] *COMPACT Composite Impact Engineering, 83 Ducie St, Manchester, M1 2JQ, UK.*

[4] *Department of Engineering Science, University of Oxford, Parks Road, Oxford, OX1 3PJ, UK.*

Abstract

A constitutive model for the rate dependent mechanical behaviour of woven composites is presented. A glass fibre composite was experimentally characterised under quasi-static and dynamic regimes to determine the strain rate dependency. Afterwards, the physical findings were used to develop a constitutive model able to predict strain rate dependent phenomena. A continuum damage mechanics approach was implemented to capture the composite failure and strain rate dependency was incorporated in the ply properties together with a damping algorithm for stability purposes. As a result, the model provided strain rate dependent behaviour while ensuring the stability of the numerical simulations. Finally, the model was used to investigate the low velocity impact response of composite plates, showing the importance of considering the strain rate dependency even at medium rates to accurately predict the response laminates subjected to dynamic loads.

1. Introduction

Composite materials are widely used for high performance structural applications in aerospace, automotive and naval industries. Their specific strength and stiffness, especially in the plane of the lamina, have contributed progressively to reduce the weight of components, resulting in economical benefits in terms of manufacturing and operational costs [44, 48]. However, when subjected to transversal loads such as those generated by impact, traditional unidirectional laminates present large delamination areas [56]. A valid alternative to improve out-of-plane performance is represented by woven composites, which even if possessing lower stiffness and strength in the plane direction, exhibit higher fracture toughness and impact tolerance [50, 38, 36]. Quasi-static response and failure modes of woven composites are well understood by the scientific community [64, 62, 35], nevertheless, little information is available regarding the behaviour at high strain rates [28, 51, 1]. Although a solid methodology to analyse the quasi-static response of woven composites has been developed over the past years [23, 33, 17, 72], the research community has not yet agreed on an

accurate strain rate dependent numerical formulation to predict the impact response. From a physical standpoint, the strain rate dependency of composite materials is attributed to the polymeric constituents, usually the matrix and some fibre types such as glass [39]. In general, higher stiffness, strength and a more pronounced non linear behaviour are found when increasing the strain rate [19, 40]. Quasi-static and dynamic failure modes are often equivalent, however, differences have been reported under compression loads, where the generation of kink bands is substituted by fibre axial splitting [38]. From a numerical view point, the major challenges are introduced by the complexity of strain rate dependent equations, as well as the correct energy dissipation when damage occurs [47].

Multiple approaches can be found in the literature predicting the impact response of composite materials. Strain rate effects of thin carbon fibre laminates subjected to low velocity impact were frequently neglected as the mechanical response of carbon fibres have no dependency with the strain rate [13, 14, 61]. At medium impact velocities, material parameters were substituted by dynamic properties [37, 52] or constant strain rates were enforced in the constitutive equations, neglecting the instantaneous strain rates induced in the plate by the impactor [24, 39]. These simplified approaches tended to fail when reproducing higher impact energy regimes, where matrix dominated failure modes control the overall response of the component [16]. To overcome such limitations, classical plasticity and viscoelastic theories were used to formulate the strain rate dependent mechanical response of composites [54, 65]. These approaches either considered the composite as an homogeneous orthotropic material [34, 55, 29] or introduced the strain rate dependency in the resin [66, 15, 11, 30, 5, 39, 57]. Although they captured the stress-strain shear curves of the laminates, they offered limited insight on the failure modes.

Nowadays efforts has been focused on the prediction of the dynamic failure modes by physically-based rate dependent failure criteria. Extension of conventional approaches can be found in the literature, incorporating the strain rate dependency into the material properties such as stiffness, strength and fracture toughness [69, 9]. The theory demonstrated how a single set of failure criteria could be formulated when using an appropriate stress transformation based on the established dependence on strain rate [21, 59, 70]. Although the formulation worked analytically, numerical issues appeared during implementation in continuum damage mechanics frameworks. Dynamic problems with localized softening are not mathematically well posed and, hence, they result in numerical instabilities [6]. After the onset of damage, the phenomenological strain softening modifies the wave propagation inducing disturbances in the stress field, which might lead to unrealistic failure of the structures [27, 12, 7].

Within this context, the present work intends to formulate a stable strain rate dependent constitutive model for woven composites to predict the impact performance of the laminates. A continuum damage mechanics approach based on a maximum stress criteria formulated over the ply properties accounts separately for the response of warp and weft yarns. Accumulated damage due to matrix cracking is phenomenologically captured by the non-linear shear response. Strain rate dependency is included in the ply properties together with a damping algorithm for stability purposes. The model is validated for a glass fibre woven composite characterised at different loading regimes to determine the strain rate de-

pendency. Dynamic testing is accomplished using a split-Hopkinson tensile bar equipment and strain fields and failure mechanisms are ascertained by means of high speed 2D Digital Image Correlation. The model is implemented in a commercial finite element software and the constitutive equations are verified at element and coupon level. Finally the constitutive model is used to simulate the dynamic response and failure of woven laminates subjected to low velocity impacts on a drop weight tower.

2. Material and experimental techniques

2.1. Material and manufacturing

For the present study, a generic glass fibre composite has been selected for validation and verification of the constitutive equations. The composite is based on pre-preg sheets of S2 glass fibres 6781 with 8-harness satin structure embedded in an epoxy resin MTM44. One cross-ply laminate composed by 8 layers with stacking sequence $[0/90]_{2s}$ was manufactured to characterise the mechanical properties. Difference between warp and weft directions were neglected during this research as no evidence of relevant differences in stiffness and strength along perpendicular directions were found in previous studies [49, 60]. The composite was cured in a hot plate press under 2 bar pressure using two different steps at 130 and 180°C of 120 min duration each. The heat-up rate was controlled during the curing cycle to avoid the risk of exothermic reactions in case of temperature overshoots. Overall thickness of the panel was quite homogeneous with a mean value of 1.75±0.15 mm on the central area and $4.56 kg/m^2$ equivalent areal weight.

Dog bone specimens with 10 mm gauge length were manufactured in a manual lathe XYZ 1400 model. Specimens were extracted from the central region of the panel to avoid the lower density areas and bonded to metallic end-caps with epoxy resin to thread them to the testing bars. Adhesive was cured 24 hours at room temperature and 60 min at 80 °C in an oven. The low strength of the adhesive increased the technical difficulties during mechanical testing and limited the width of the specimens set as 5 and 4 mm for tensile and shear tests respectively, see Fig. 1.

2.2. Quasi-static characterisation

Quasi-static tests were accomplished with the actuator of a Zwick screw-driven testing frame. Tensile tests were carried out under stroke control at cross head speed of 0.001 mm/s at a strain rate of $10^{-4} s^{-1}$ over 10 mm gauge length. The load was recorded continuously with a 20kN load cell together with the cross-head displacement of the testing frame. Additionally, laser extensometer was used to acquire the longitudinal displacement of the gauge section during the test with a vertical scale of 50 mm and a working distance of 381 mm.

2.3. Dynamic characterisation

Dynamic tests were carried out with an in-house designed and manufactured split-Hopkinson bar for high rate tensile test located at the University of Oxford. The apparatus is composed by loading, input and output bars and the specimen is mechanically gripped between the input and the output bars. The loading bar is pulled by a striker impulsed

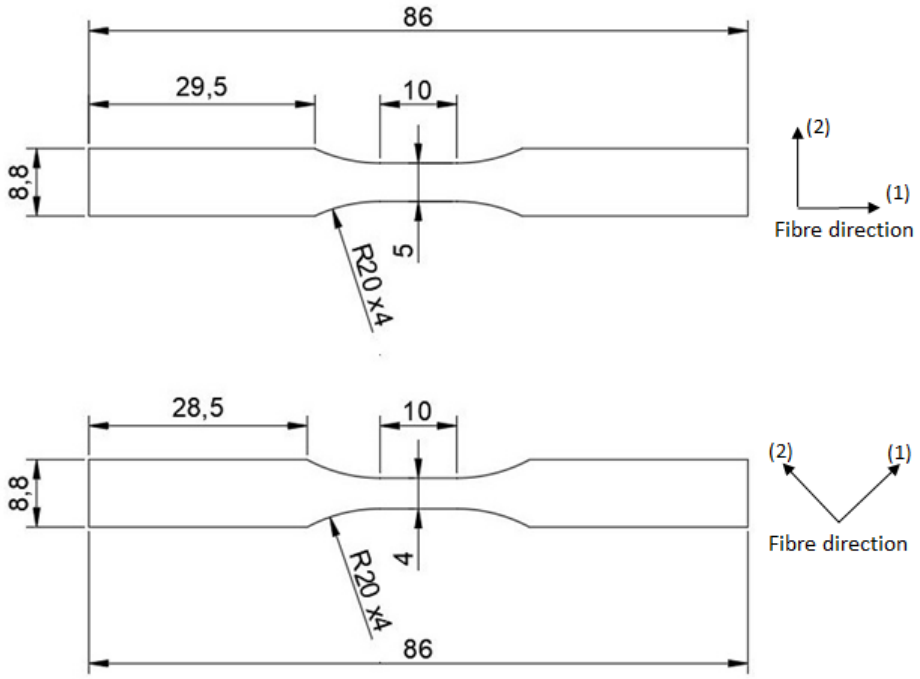

Figure 1: Dimensions of the coupons used for the mechanical characterisation with 10 mm gauge length. (a) Specimen for tensile tests, with 5 mm width and (b) Specimen for shear tests, with 4 mm width.

by low-pressure air to produce a tensile pulse which propagates along the input bar. When the incident pulse reaches the end of the input bar, part of this pulse is transmitted into the specimen and, afterwards, into the output bar. Axial strain gauges are mounted on the surfaces of the input and output bars providing time-resolved measurements of the travelling elastic pulses. The strain of the bars are used to obtain the stress-strain curves of the specimens following the data treatment in [41].

Measuring the high strain rate tensile and shear response of woven composites presents considerable technical difficulties associated to the transit time to achieve dynamic force equilibrium and to the large strains to failure. To overcome these difficulties, long projectile and bars were used in the proposed set up. Loading bar of 3.6 m length and 20 mm diameter surrounded by a 2.5 m striker with a U shaped cross/section of 35 mm diameter were chosen together with 16 mm diameter input and output bars of 3 m length approximately. All bars were manufactured in Titanium alloy Ti-6Al-4V and supported by low friction polymeric bearings to prevent bending. The striker was accelerated up to 10 m/s to reach 1000 s^{-1} strain rate over 10 mm gauge length. The long projectile let to a pulse length of 1 ms duration, resulting in large applied strains. In order to ensure force equilibrium, the shape of the pulse was modified using a 1 mm thickness neoprene foam as pulse shaper, increasing the rising time and decreasing the wave dispersion and high-frequency oscillations of the system. Detailed description of the experimental set-up can be found in [26].

Full field displacement measurements in the specimen were carried out by high-speed

Material Property \ Strain rate	10^{-4} s^{-1}	400 s^{-1}
Young's Modulus (GPa) (E_T)	22.6±0.5	21.1±3.7
Tensile strength (GPa) (σ_T)	0.49±0.04	0.79
Poisson's ratio (ν_{12})	—	0.375±0.053

Table 1: In-plane tensile mechanical properties of the glass fibre composite as a function of the strain rate.

Material Property \ Strain rate	10^{-4} s^{-1}	900 s^{-1}
Shear Modulus (GPa) (G_{12})	4.3±1.15	—
Shear Yield Strength (GPa) (S_{12}^{yield})	0.043±0.005	—
Shear Strength (GPa) (S_{12})	0.13±0.02	0.17±0.03

Table 2: In-plane shear mechanical properties of the glass fibre composite as a function of the strain rate.

photography with an ultra-high-speed Kirana camera at 400.000 fps and 924 x 768 pixels resolution. 2D Digital Image Correlation (DIC) using the software GOM-Correlate was performed [31]. Specimens were speckled with white and black paintings to capture the local strain field during the mechanical tests. Given the camera resolution and the pattern sizes, window size and distance were selected as 19 and 16 pixels respectively, to ensure the overlapping of the facets. Strains were afterwards calculated using an spatial average filter and a temporal smoothing spline with a manual tolerance of 0.1%. More details about the experimental technique can be found in [45].

3. Mechanical properties

Quasi-static and dynamic tensile and shear responses of the material were characterised following the methodology presented in previous section. Three quasi-static and five dynamic tests were accomplished for each configuration, reaching 400 s^{-1} and 900 s^{-1} strain rates for tensile and shear specimens respectively. Applied strain rate for tensile tests was lower to ensure dynamic force equilibrium was achieved before the failure of the material, at approximately 1% and 4% deformation for tensile and shear tests respectively.

The tensile response of the material was linear elastic up to the onset of damage, with a remarkable strain rate dependency in terms of tensile strength, with 160% increment under dynamic loads. Stiffness along the principal direction presented no strain rate dependency. Representative nominal stress *vs.* engineering strain curves for tensile tests are plotted in Fig. 2 and the average values and standard error of the young modulus, E_T, nominal tensile strength, σ_T, and in-plane Poisson's ratio ν_{12} for the different strain rates are depicted in Table 1. Due to the high applied forces and the technical complexity of the tensile tests, only one single specimen achieved the final strength, while the rest of the samples failed due to debonding of the specimen-endcap interface. These results are in accordance with

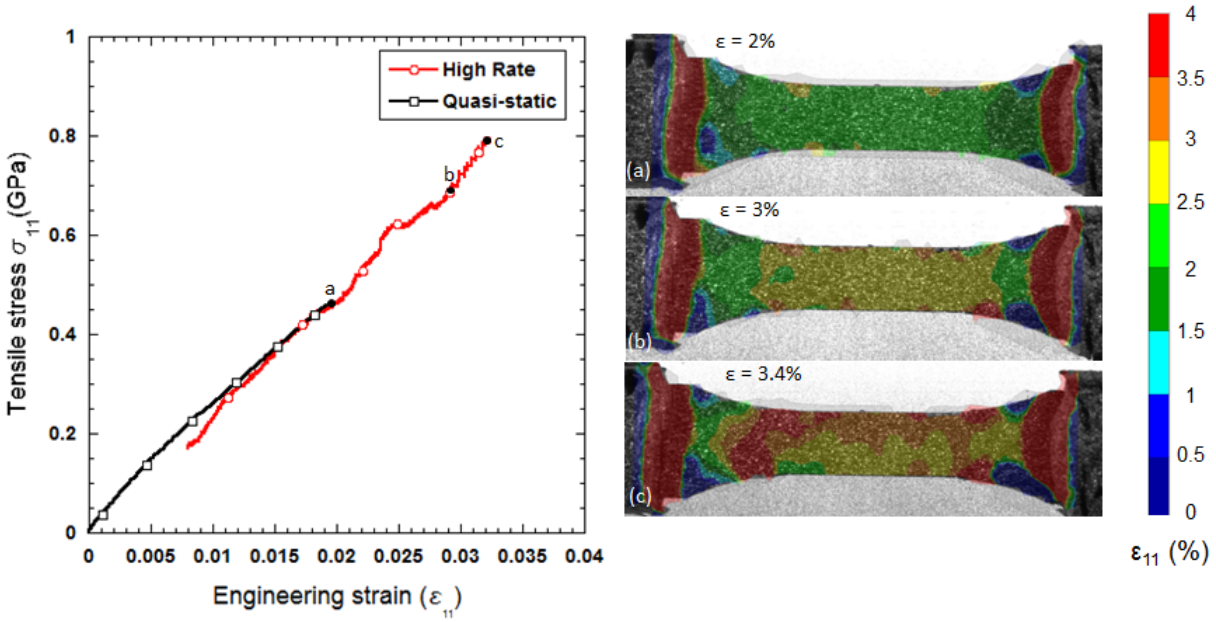

Figure 2: Tensile response of the glass fibre composite. On the left hand side, representative engineering stress *vs* engineering strain curves at quasi-static 10^{-4} s^{-1} and high strain rate 400 s^{-1}. On the right hand side, contour plots of the dynamic engineering strain in the loading direction at different applied strains. (a) 2% deformation, (b) 3% deformation and (c) 3.4% deformation.

previous investigations in the dynamic response of glass fibres [3], therefore, the strain rate dependency of the composite has been attributed to the glass fibre nature instead of the woven architecture and the yarn waviness. Deformation and failure mechanisms were analysed for different stages (points a, b and c in the stress-strain curve) in the right hand side of Fig. 2 by 2D digital image correlation. The composite presented a homogeneous strain field for all deformation levels before damage localisation, where cracks developed perpendicular to the loading direction at the region which presented the change of curvature, see Fig. 2(c). As a result of stress triaxiality, a possible error in the measured strength needs to be considered. Effects of the geometry on the stress state will be investigated numerically in the next sections.

The in-plane shear response was obtained from the off-axis tests transforming the applied stress and strain from the global coordinate system (xx) into the material coordinate system (12) considering the fibre orientation with respect to the testing direction, β, following:

$$\tau_{12} = \sigma_{xx} \sin\beta \cos\beta \,(1 + \varepsilon_{xx}) \tag{1}$$

$$\gamma_{12} = \varepsilon_{xx} \sin 2\beta - \varepsilon_{yy} \sin 2\beta + \gamma_{xy} \cos 2\beta \tag{2}$$

These equations are strictly valid for small deformations and limited fibre realignment. For the particular case of pure shear tests $\beta = 45°$and accounting for the change in cross-section [19]:

$$\tau_{12} = \frac{\sigma_{xx}}{2} (1 + \varepsilon_{xx}) \tag{3}$$

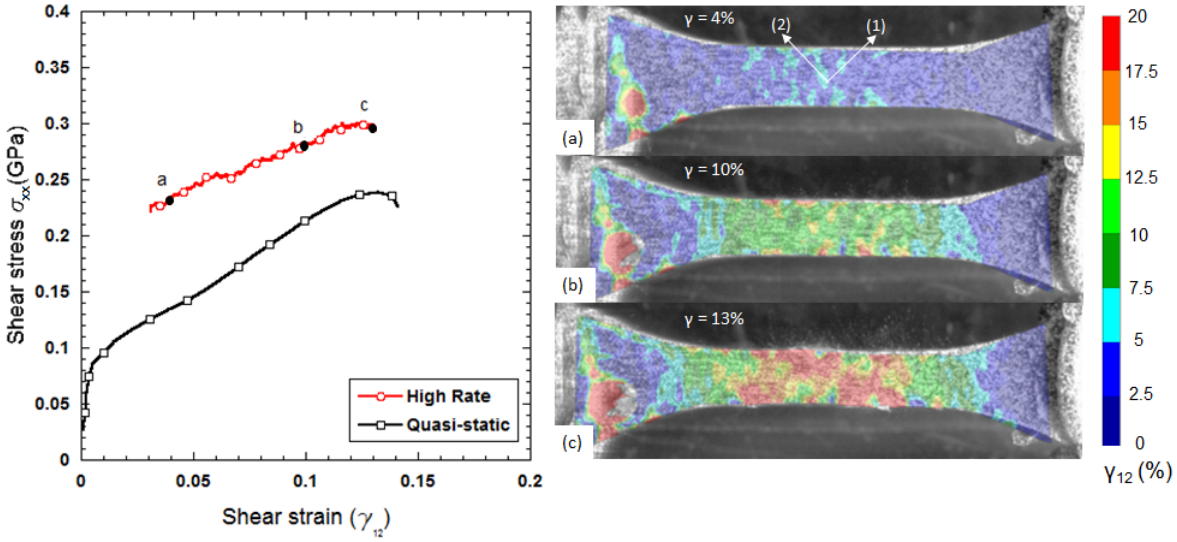

Figure 3: Shear response of the glass fibre composite. On the left hand side, representative engineering stress *vs* engineering strain curves at quasi-static strain rates 10^{-4} s^{-1} and high strain rate 900 s^{-1}. On the right hand side, contour plots of the engineering strain in the loading direction at different applied strains. (a) 4% deformation, (b) 10% deformation and (c) 13% deformation. (1) and (2) stands for the main laminate principal directions.

$$\gamma_{12} = \varepsilon_{xx} - \varepsilon_{yy} \tag{4}$$

The shear response of the composite showed the characteristic bi-linear curve formed by two different stages; a first initial elastic part followed by a second region with lower stiffness. Shear strength was also strain rate dependent, with a moderate strength increment of the 130%. No data was obtained for the initial stage under dynamic conditions as force equilibrium was achieved for a global deformation of 4%. Representative nominal stress *vs.* engineering strain curves for shear tests are plotted in Fig. 3 and the average values and standard error of the young modulus, E_T, nominal tensile strength, σ_T, and the shear modulus, G_{12}, shear yield strength, S_{12}^{yield}, and final shear strength, S_{12}, are shown in Table 2. Deformation and failure mechanisms for the different stages (points a, b an c in left hand side Fig. 3) were analysed by 2D digital image correlation. The full-field of the engineering strain along the loading axis is shown in the right hand side of Fig. 3. Homogeneous strain was also appreciated during the loading process. After reaching the yielding strain, progressive deformation induced matrix cracking, decreasing the stiffness of the material and generating strain concentration on the edges of the dogbone specimen, see Fig. 3(b). Further deformation resulted in multiple cracks propagating along the 45°orientation, see Fig. 3(c). Finally the maximum load capacity of the material was achieved, macro-cracks propagated along the central region of the specimen and yarns were sequentially pulled-out, see Fig. 4. No yarn breakage was appreciated due to the geometrical characteristics of the specimen, which did not constraint the yarns at their endings as suggested by the standard test method for in-plane shear tests of polymer matrix composites by tensile tests [4] .

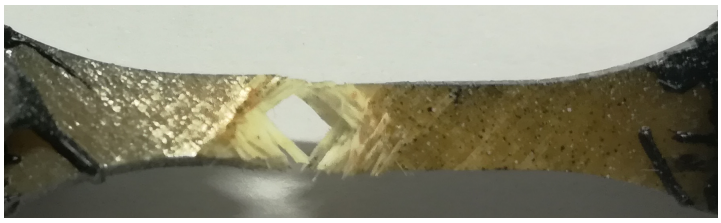

Figure 4: Post-mortem shear specimen. Matrix was totally damaged and yarns were pulled-out from the layers, resulting in the catastrophic failure of the material.

4. Constitutive model

The model presented in this section provides the constitutive response of a woven composite subjected to in-plane loads, accounting for the main failure micromechanisms (yarn tensile and compression failure, and matrix cracking) with emphasis on the non-linear strain rate dependent shear response. To obtain a good prediction of the damage evolution, a continuum damage mechanics approach defines separately the response of the warp, weft yarns and matrix cracking. Evolution of damage is implemented by a phenomenological softening function controlled by the fracture toughness of the material at each particular direction. Non linear in-plane shear response is implemented with a time efficient algorithm that follows the evolution of the permanent deformation and can be implemented in explicit integration schemes, decreasing the computation cost of the simulation. The model is intended to be used within the framework of explicit finite element method and provides the constitutive response for a mesodomain of the composite at lamina level corresponding to the volume associated to a finite element. Strain rate dependency is implemented in the ply properties together with a damping algorithm for stability purposes.

4.1. Intralaminar damage model

The model is based on the continuum damage mechanics theory for anisotropic solids [42] and the principle of progressive failure of Hashin [32]. The mechanical response is considered linear elastic up to the onset of damage except for the in-plane shear response, which is defined non-linear inelastic up to the onset of damage. The compliance matrix (the relation between stress and strain tensors) is given, in Nye's notation, such as:

$$\begin{bmatrix} \varepsilon_1 \\ \varepsilon_2 \\ \varepsilon_3 \\ \gamma_{31} \\ \gamma_{23} \\ \gamma_{12} \end{bmatrix} = \begin{bmatrix} \frac{1}{(1-d_1)\,E_1} & -\frac{\nu_{12}}{E_1} & -\frac{\nu_{31}}{E_1} & 0 & 0 & 0 \\ -\frac{\nu_{12}}{E_1} & \frac{1}{(1-d_2)\,E_2} & -\frac{\nu_{23}}{E_2} & 0 & 0 & 0 \\ -\frac{\nu_{31}}{E_1} & -\frac{\nu_{23}}{E_2} & \frac{1}{E_3} & 0 & 0 & 0 \\ 0 & 0 & 0 & \frac{1}{G_{31}} & 0 & 0 \\ 0 & 0 & 0 & 0 & \frac{1}{G_{23}} & 0 \\ 0 & 0 & 0 & 0 & 0 & \frac{1}{f\,(d_{12}, d_{12}^{pp})} \end{bmatrix} \begin{bmatrix} \sigma_1 \\ \sigma_2 \\ \sigma_3 \\ \tau_{31} \\ \tau_{23} \\ \tau_{12} \end{bmatrix} \tag{5}$$

where $E_1, E_2, E_3, \nu_{12}, \nu_{23}, \nu_{31}, G_{31}$ and G_{23} are the 8 independent elastic constants which determine the behaviour of the undamaged orthotropic material in the local axis orientation and $f\,(d_{12}, d_{12}^{pp}, \gamma_{12})$ is the function which dictates the non-linear in-plane shear stress. Main direction (X-1) stands for the warp yarns and perpendicular direction (Y-2) stands for weft yarns.

As the maximum strength along each direction is reached, a softening law defines the post-peak behaviour dominated by the material fracture energy. The elastic compliance matrix of the composite material is modified in terms of damage variables $d_1, d_2, d_{12}, d_{12}^{pp}$ which control the evolution of damage during an arbitrary loading path.

4.1.1. Yarn tensile and compression failure criteria

Yarn breakage due to tensile and compression stresses are accounted by the damage variables d_1 and d_2 that modify the stiffness tensor by decreasing the overall stress of the mesodomain following the Lemaitre continuum damage model [42]. Damage variables are controlled by lamina stresses of each individual plies. The onset and propagation of damage is established by the damage activation function, F_M, expressed as:

$$F_M = \phi_M - r_M \tag{6}$$

where ϕ_M is the damage surface and r_M is the damage threshold, an internal variable of the model which is initially equal to 1. The sub-index M stand for the failure modes, tensile and compression failure along the principal fibre directions 1 and 2. Damage develops when $F_M = 0$ and $\dot{\phi}_M > 0$, thus, the evolution of damage is controlled by the consistency condition that establishes:

$$\dot{F}_M = \dot{\phi}_M - \dot{r}_M = 0 \Rightarrow \dot{r}_M = \dot{\phi}_M \tag{7}$$

When the damage threshold r_M evolves, the damage variables d_M become active to ensure a correct energy dissipation after the onset of damage. The damage variables increase monotonically with the damage threshold. The onset of damage is defined by a maximum

stress criterion previously validated for 3D woven composites and briefly recalled in this section for the shake of completion [49]. The mathematical expressions of the failure functions, F_M, and the damage surfaces, ϕ_M, used to trigger the onset of damage by reaching the damage thresholds, r_M, are expressed as:

$$F_M = \phi_M - r_M = \frac{E_i}{X_M}\varepsilon_i - r_M = 0 \tag{8}$$

where E_i stand for the ply stiffness, X_M, for the ply strength and ε_i for the applied strain. The maximum values of the damage thresholds under tensile and compressive loads are stored to be used as the new updated damage thresholds.

As the failure stress is reached and the damage threshold evolves, a softening law defines the material post-peak behaviour introduced by the damage variable d_M dominated by the material fracture energy Γ_M. Exponential damage evolution is formulated according to:

$$d_M = 1 - \frac{1}{r_M} exp[A_M(1 - r_M)] \tag{9}$$

where the parameter A_M ensures that the energy dissipated during fracture is independent of the characteristic length of the finite element l_{ch} used for the discretization [8]. The softening parameters, A_M, can be approximated by the analytical expression:

$$A_M = \frac{2 l_{ch} X_M^2}{2 E_i \Gamma_M - l_{ch} X_M^2} \tag{10}$$

With the previous methodology the damage variables for the current loading states $d_{1+}, d_{1-}, d_{2+}, d_{2-}$ are obtained. After that, the consistency condition eq.7 is used to ensure damage variables for each failure mode M increase with the evolution of the damage threshold r_M. Finally, the damage variables in equation 5 take into account the load directionality. Then, the warp and weft damage variables for each material direction d_1 and d_2 are defined:

$$d_1 = d_{1+}\frac{<\sigma_{11}>}{|\sigma_{11}|} + d_{1-}\frac{<-\sigma_{11}>}{|\sigma_{11}|} \tag{11}$$

$$d_2 = d_{2+}\frac{<\sigma_{22}>}{|\sigma_{22}|} + d_{2-}\frac{<-\sigma_{22}>}{|\sigma_{22}|} \tag{12}$$

where $< \bullet >$ is the Macaulay operator (positive part) which returns the argument if positive and zero otherwise.

4.1.2. In-plane non linear shear response

The constitutive model also includes the intrinsic in-plane non-linear shear response of textile composites as characterised in previous sections. Representative stress-strain curve is plotted in Fig. 5(a). An initial linear elastic part followed by a potential curve has been chosen to ensure stability in the transition zone and a monotonic increment of stress with the strain. The curve is fully defined by four material parameters: the initial elastic shear

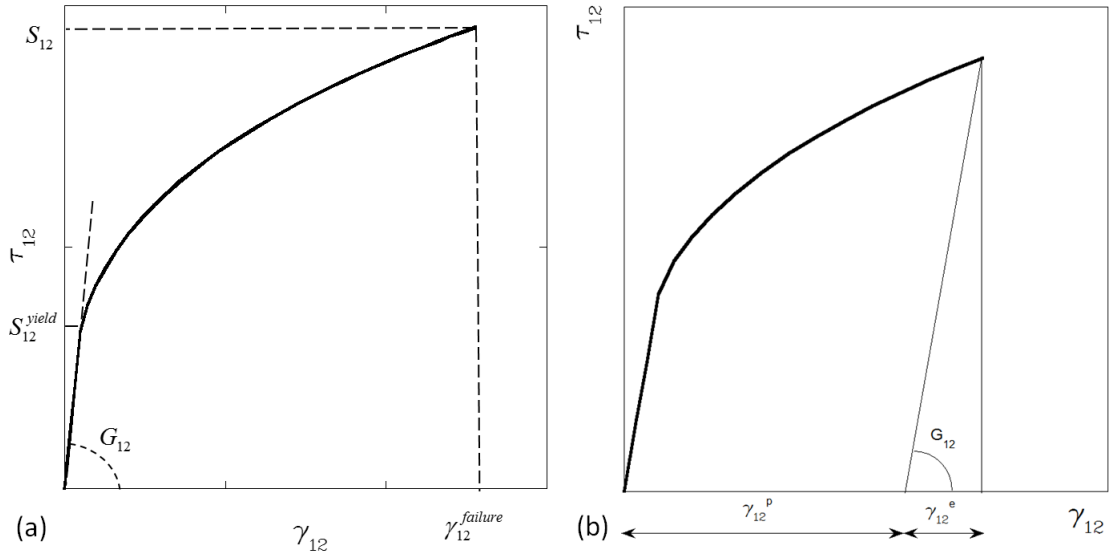

Figure 5: Non-linear stress-strain in-plane shear response. (a) Material parameters: elastic shear modulus, G_{12}, yielding strength, S_{12}^{yield}, shear strain to failure, $\gamma_{12}^{failure}$, and maximum shear strength, S_{12}. (b) Permanent shear deformation, γ_{12}^{p}, and elastic shear deformation, γ_{12}^{e}.

modulus, G_{12}, the yielding shear strength, S_{12}^{yield}, the shear strain to failure, $\gamma_{12}^{failure}$, and the maximum shear strength, S_{12}.

To keep track of the deformation history under cyclic loadings, the non-linear shear response is implemented from an internal variable so called accumulated shear strain γ_{12}^{accum}, which accounts for the load-time history. It is computed in incremental formulation such that:

$$\gamma_{12}^{accum,t} = \gamma_{12}^{accum,t-1} + \varsigma \cdot \Delta\gamma_{12}^{t} \tag{13}$$

where the index t refers to the current time step, the index $t-1$ recalls for the previous time step, $\Delta\gamma_{12}^{t}$ is the current increment of shear strain and ς is a function which accounts for the tensile or compression state of the load expressed in incremental formulation according to:

$$\varsigma = \frac{\tau_{12}^{t-1} + \Delta\gamma_{12}^{t} G_{12}}{|\tau_{12}^{t-1} + \Delta\gamma_{12}^{t} G_{12}|} \tag{14}$$

where τ_{12}^{t-1} is the shear stress at the previous time step. Both variables result in good convergence for small time increments and, therefore, the formulation is suitable for explicit integration schemes.

The proposed constitutive model is divided in two different stages: an initial linear elastic response up to the yielding strength, S_{12}^{yield}, and a second non-linear inelastic mechanical response:

$$\tau_{12} = \varsigma G_{12} |\gamma_{12}^{accum}| \qquad if \;\; |\gamma_{12}^{accum}| < \gamma_{12}^{yield} \tag{15}$$

$$\tau_{12} = \varsigma h |\gamma_{12}^{accum}|^{n} \qquad if \;\; |\gamma_{12}^{accum}| > \gamma_{12}^{yield} \tag{16}$$

where γ_{12}^{yield} is the strain at the yielding point defined as:

$$\gamma_{12}^{yield} = \frac{S_{12}^{yield}}{G_{12}} \tag{17}$$

and h and n are the coefficients of the potential relation expressed as:

$$n = \frac{log\frac{S_{12}^{yield}}{S_{12}}}{log\frac{\gamma_{12}^{yield}}{\gamma_{12}^{failure}}} \tag{18}$$

$$h = \frac{S_{12}}{\left(\gamma_{12}^{failure}\right)^n} \tag{19}$$

To account for the permanent deformations, the non linear shear response is formulated following the methodology used for the damage evolution in the previous section. The evolution of the non linear inelastic response is controlled by the yielding activation function, F_{12}^{yield}, such that:

$$F_{12}^{yield} = \phi_{12}^{yield} - r_{12}^{yield} = h|\gamma_{12}^{accum}|^n - r_{12}^{yield} \tag{20}$$

where ϕ_{12}^{yield} is the yield surface and r_{12}^{yield} is the yield threshold which takes the initial value of the yield strength S_{12}^{yield}. Non linear inelasticity develops when $F_{12}^{yield} = 0$ and $\dot{\phi}_{12}^{yield} > 0$ following the consistency condition:

$$\dot{F}_{12}^{yield} = \dot{\phi}_{12}^{yield} - \dot{r}_{12}^{yield} = 0 \Rightarrow \dot{r}_{12}^{yield} = \dot{\phi}_{12}^{yield} \tag{21}$$

therefore, the yield threshold is continuously updated and increases monotonically during the loading process.

Every time step, the model calculates an elastic stress predictor, which is compared against the updated yield surface resulting in the following loading and unloading processes schematically represented in Fig. 6(a) and (b) according to:

$$\tau_{12} = \varsigma \cdot h|\gamma_{12}^{accum}|^n \qquad if \;\; \phi_{12}^{yield} > r_{12}^{yield} \tag{22}$$

$$\tau_{12} = \varsigma \cdot G_{12} \cdot (|\gamma_{12}^{accum}| - \gamma_{12}^{p}) \qquad if \;\; \phi_{12}^{yield} < r_{12}^{yield} \tag{23}$$

where γ_{12}^{p} is the permanent deformation caused by the inelastic response of the material during previous loading states.

In this model permanent deformations are considered in absolute value and are computed from the absolute value of the applied strain. It is schematically represented in Fig. 5(b). The permanent deformation is directly obtained by the subtraction of the maximum historic elastic recoverable strain, $\gamma_{12}^{e}(r_{12}^{yield})$, to the total applied strain on the previous time step:

$$\gamma_{12}^{p} = |\gamma_{12}^{accum}| - \frac{r_{12}^{yield}}{G_{12}} \tag{24}$$

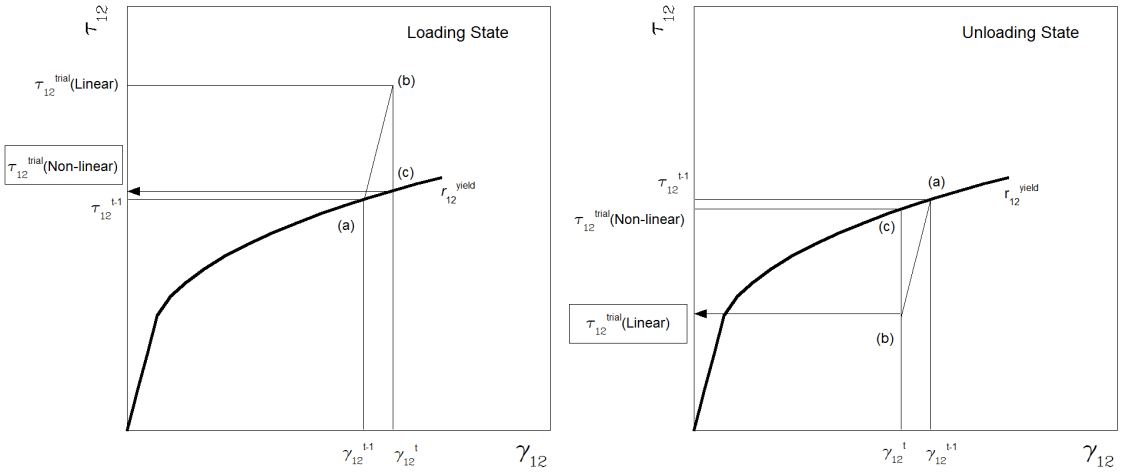

Figure 6: Mechanical response of the non-linear inelastic model implemented for the definition of the shear response under (a) loading and (b) unloading conditions. The model updates the yield surface and compares it with the yield threshold. In case the yield threshold is overtaken (figure a), the final trial stress is given by the yield function, equation 22, otherwise (figure b), the value computed by the elastic stress predictor is maintained, equation 23.

For a better visualization of the proposed formulation, Fig. 7(a) shows a tension-compression loading case and Fig. 7(b) the respective shear strain, γ_{12}, accumulated strain, γ_{12}^{accum}, and the strain corresponding to the current yielding threshold, $\gamma_{12}\left(r_{12}^{yield}\right)$. During the first loading stage, the yielding strength, S_{12}^{yield}, is overtaken and the material reaches the stress value $\tau_{12}(A)$. As there are no changes in the sign of the stress function (in this particular case, positive $\varsigma = 1$, eq. 14), the accumulated strain agrees with the shear strain of the mesodomain, $\gamma_{12}^{accum} = \gamma_{12}$. Afterwards a compression loading is applied. Given the permanent deformation, a linear elastic response is obtained from point A to point C, crossing the zero stress at point B. The shear strain, γ_{12}, imposed in the mesodomain decreases and so does the accumulated shear strain up to point B, where the change of the ς function (negative $\varsigma = -1$) modifies the value of the accumulated strain so $\gamma_{12}^{accum} \neq \gamma_{12}$. At point C, the yielding surface is reached again, $\phi_{12}^{yield} = r_{12}^{yield}$, resulting in the previous stress state $\tau_{12}(A) = -\tau_{12}(C)$ and $\gamma_{12}^{accum} = \gamma_{12}\left(r_{12}^{yield}\right)$. Finally, compression increases, causing the monotonic evolution of the yield threshold r_{12}^{yield} following the consistency equation.

4.1.3. Matrix cracking

Debonding and matrix cracking are initiated inside yarns oriented perpendicular towards the loading direction for relative low tensile strains [20]. Although this failure mode does not have any influence in the tensile response of the composite along the loading direction, mainly supported by the principal oriented yarns, it clearly degrades the shear response. In the literature there are available experimental studies analysing the degradation of woven composites subjected to shear cyclic loading, relating the loss of stiffness to the evolution of crack density [68, 66]. This assumption has been previously considered in numerical

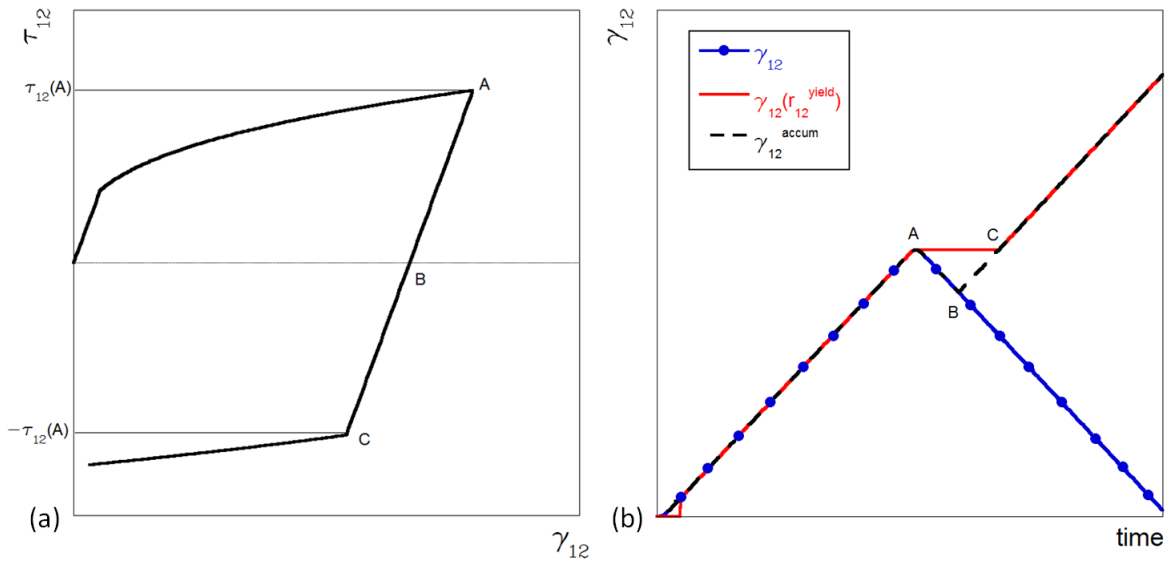

Figure 7: Tension-compression shear loading cycle. (a) Stress-strain curve, with symmetrical hardening response and $\tau_{12}(A) = -\tau_{12}(C)$ computed from the accumulated shear strain, γ_{12}^{accum}. (b) Respective shear strain, γ_{12}, strain at the current yielding threshold, $\gamma_{12}\left(r_{12}^{yield}\right)$, and accumulated strain, γ_{12}^{accum}.

simulations to reproduce the permanent deformation and the non linear shear response of woven composites [15, 17].

Assuming same failure mode appears during dynamic events, the present constitutive model includes the yarn debonding and matrix cracking by the damage variable d_{12}, that modifies the shear stiffness according to equation 5 following the Lemaitre continuum damage model presented in the previous section. As analysed experimentally, only perpendicular tensile stresses contribute to the matrix cracking [20], therefore, the present expression is proposed as activation function for the shear failure mode, accounting for both, the cracking of warp and weft yarns:

$$F_{12} = \phi_{12} - r_{12} = \frac{\sqrt{\left(E_1 <\varepsilon_1>\right)^2 + \left(E_2 <\varepsilon_2>\right)^2}}{N} - r_{12} = 0 \tag{25}$$

where N is the normal interface strength. Once the activation function becomes higher than 1, the damage variable d_{12} evolves following the expression:

$$d_{12} = 1 - \frac{1}{r_{12}} exp[A_{12}(1 - r_{12})] \tag{26}$$

where the softening parameter A_{12} is calculated over a conservative virtual shear curve according to:

$$A_{12} = \frac{2 l_{ch} N^2}{2 G_{12} \Gamma_{12} - l_{ch} N^2} \tag{27}$$

to ensure the energy dissipated over the shear direction does not exceed the shear fracture toughness Γ_{12}.

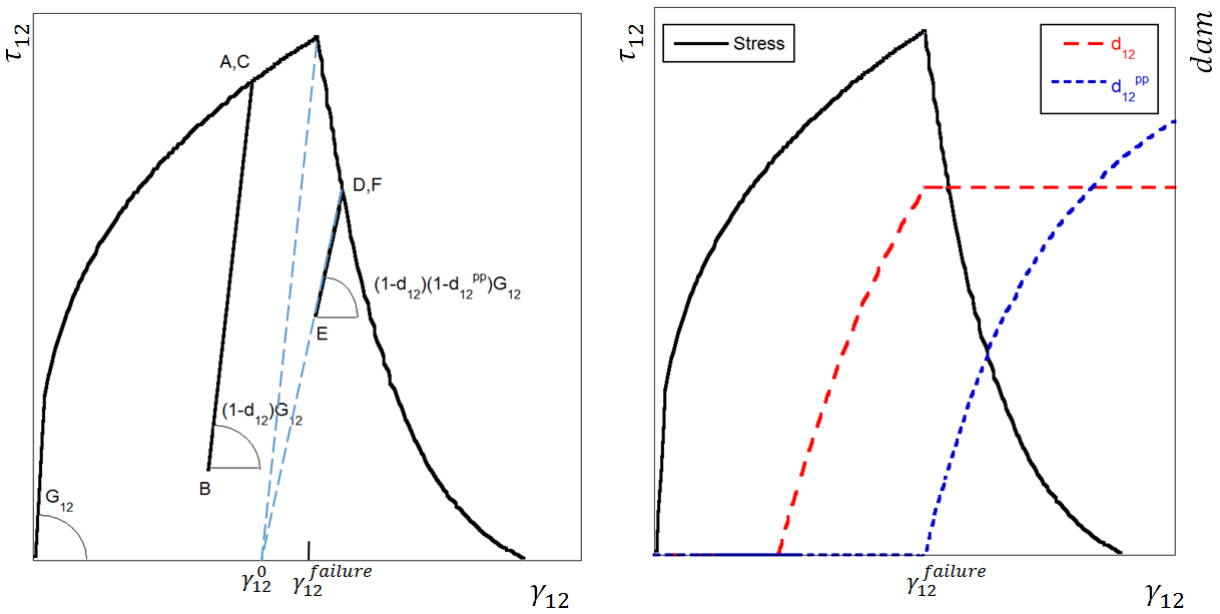

Figure 8: Progressive degradation of the shear modulus due to matrix cracking. (a) Cyclic loading and difference in slope during unloading of shear stresses. The first unloading (A-B-C) presents degradation due to yarn cracking implemented through the damage variable d_{12}, while the second unloading during the post-peak response (D-E-F) presents a softening controlled by the damage variable d_{12}^{pp} which ensures the total dissipated energy due to shear failure is equal to the fracture toughness. (b) Evolution of the damage variables with the shear deformation. Once the shear strength is achieved, the damage post-peak damage variable d_{12}^{pp} initiates its evolution, while the initial damage variable d_{12} gets frozen.

The accumulated damage induces a degradation of the shear modulus schematically depicted by the cyclic loading (A-B-C) in Fig.8(a). It causes permanent deformations along shear direction defined by:

$$\gamma_{12}^{p} = |\gamma_{12}^{accum}| - \frac{r_{12}^{yield}}{(1-d_{12})G_{12}} \tag{28}$$

and analytically, the shear stiffness is modified including the damage variable such that:

$$\tau_{12} = \varsigma\,(1-d_{12})\,G_{12}\,(|\gamma_{12}^{accum}| - \gamma_{12}^{p}) \tag{29}$$

When the material exceeds the maximum shear strength $\tau_{12} > S_{12}$, an exponential softening law drives the post-peak behaviour. In order to re-use the previous approach, a simple correction of the applied strain γ_{12}^{dam} can be included:

$$\gamma_{12}^{dam} = \gamma_{12}^{acumm} - \gamma_{12}^{failure} + \frac{S_{12}}{(1-d_{12})\,G_{12}} \tag{30}$$

thus a new reference strain γ_{12}^{0} is virtually created, equivalent to the zero strain of a linear elastic response, see Fig.8(a). At this point, the shear damage variable d_{12} does not suffer further evolution, see Fig.8(b), and the remaining post-peak energy of the shear failure mode

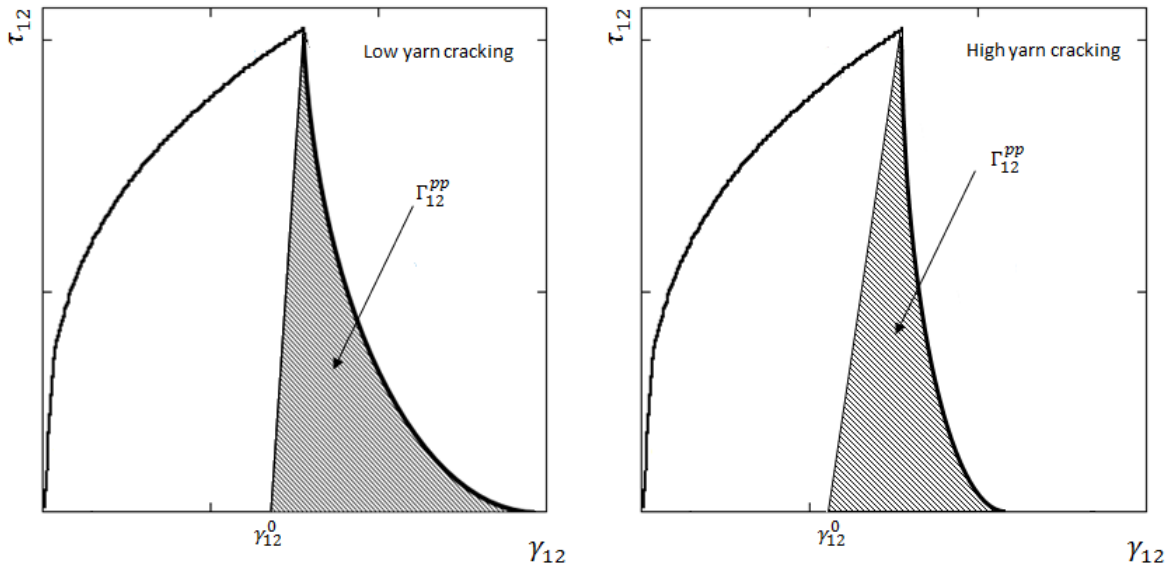

Figure 9: Shear response after the onset of damage controlled by the post peak fracture toughness Γ_{12}^{pp} given by eq.31. (a) Low and (b) high yarn cracking, resulting in ductile and brittle post-peak responses respectively.

is calculated subtracting the dissipated energy to the total fracture toughness:

$$\Gamma_{12}^{pp} = \Gamma_{12} - l_{ch}\left(\frac{d_{12}}{1-d_{12}}\right)\frac{S_{12}^2}{2G_{12}} \tag{31}$$

The exponential curve is afterwards defined by the post-peak shear damage variable d_{12}^{pp}, which is equal to 0 at the onset of failure and evolves following a post-peak damage threshold r_{12}^{pp}, see Fig.8(b), defined by the activation function:

$$F_{12}^{pp} = \phi_{12}^{pp} - r_{12}^{pp} = \frac{\tau_{12}^{trial}}{S_{12}} - r_{12}^{pp} = 0 \tag{32}$$

Post-peak damage evolution is, therefore, implemented following the methodology exposed before, and the softening parameter parameter A_{12}^{pp} is approximated by the analytical expression:

$$A_{12}^{pp} = \frac{2l_{ch}S_{12}^2}{2\left(1-d_{12}\right)G_{12}\Gamma_{12}^{pp} - l_{ch}S_{12}^2} \tag{33}$$

hence, final expression for the shear stress in the damaged state results in:

$$\tau_{12} = \varsigma \cdot \left(1-d_{12}\right)\left(1-d_{12}^{pp}\right)G_{12}\gamma_{12}^{dam} \tag{34}$$

Using this approach, it is possible to compute the post-peak response of the composite along the shear direction ensuring the energy dissipated is equal to the fracture toughness. Figure 9 shows the regularisation of the energy dissipated Γ_{12}^{pp} as computed in equation

31. Depending on the interface strength of the material N, yarn cracking will be initiated at different stress levels, resulting in distinct crack density before reaching the maximum strength of the material. Figure 9 shows two cases for (a) low and (b) high interface strengths. High interface strength will result in a low yarn cracking causing lower degradation of the shear stiffness (e.g. dissipating around a 25% of the total energy Γ_{12}), and therefore, high ductility during the post-peak response (releasing the remaining 75% of the energy). On the other hand, low interface strength, will result in a high yarn cracking (e.g. dissipating around a 75% of the total energy Γ_{12}) and brittle failure along the shear direction (realising the remaining 25% of the energy of the system).

4.1.4. Strain rate dependency

Strain rate dependency is directly included in the ply properties such as stiffness, strength and fracture toughness. Relationship between the updated ply properties and the strain rate is given by the following expression suggested in [71]:

$$\Lambda_M = \Lambda_M^0 \left(1 + \sqrt{\kappa_M |\dot{\varepsilon_i}^{eq}|}\right) \tag{35}$$

where Λ_M is the rate-dependent ply property (stiffness or strength) at the equivalent strain rate $\dot{\varepsilon_i}^{eq}$, Λ_M^0 is the quasi-static ply property and κ_M is the rate-dependent coefficient, which dimensionally is written in time units. The coefficient M corresponds to the failure modes 1+, 2+, and 12, associated to tensile and shear failure.

To avoid the intrinsic oscillations of dynamic simulations, a damper algorithm is employed to compute the equivalent strain rate $\dot{\varepsilon_i}^{eq}$ defined by:

$$\dot{\varepsilon_i}^{eq,t} = \dot{\varepsilon_i}^{eq,t-1}\xi + \dot{\varepsilon_i}^{t}\left(1 - \xi\right) \tag{36}$$

where ξ is the applied adimensional damping, $\dot{\varepsilon_i}^{eq,t-1}$ is the equivalent strain rate in the directly previous step and $\dot{\varepsilon_i}^{t}$ is the strain rate in the current step given by:

$$\dot{\varepsilon_i}^{t} = \frac{\Delta\varepsilon_i}{\Delta t} \tag{37}$$

When $\xi = 0$, the strain rate from the current step is used to compute the ply properties, however, when the damper ξ has a value close to 1.0, a smooth strain rate curve is obtained. This methodology considerably reduces the noise of stress free directions, without causing a significant decrement of the mechanical response of the directly loaded directions. An example of the overall improvement of the dynamic response is shown in Fig. 10 for intermediate strain rate 10 s^{-1} (upper row) and high strain rate 1000 s^{-1} (lower row). The model is subjected to a tensile load along the principal direction (1), while the perpendicular direction (2) is stress free. Negligible difference in the computed strain rate with or without damping is appreciated for the directly loaded direction and the beneficial effect of the damping algorithm appears when measuring the strain rate over the perpendicular direction (2). The pure numerical explicit algorithm ($\xi = 0$) results in a noisy response over the unloaded direction, that involves numerical instabilities and unphysical failure of the material. The damping algorithm alleviates the numerical issue, resulting in a stable formulation of the strain rate.

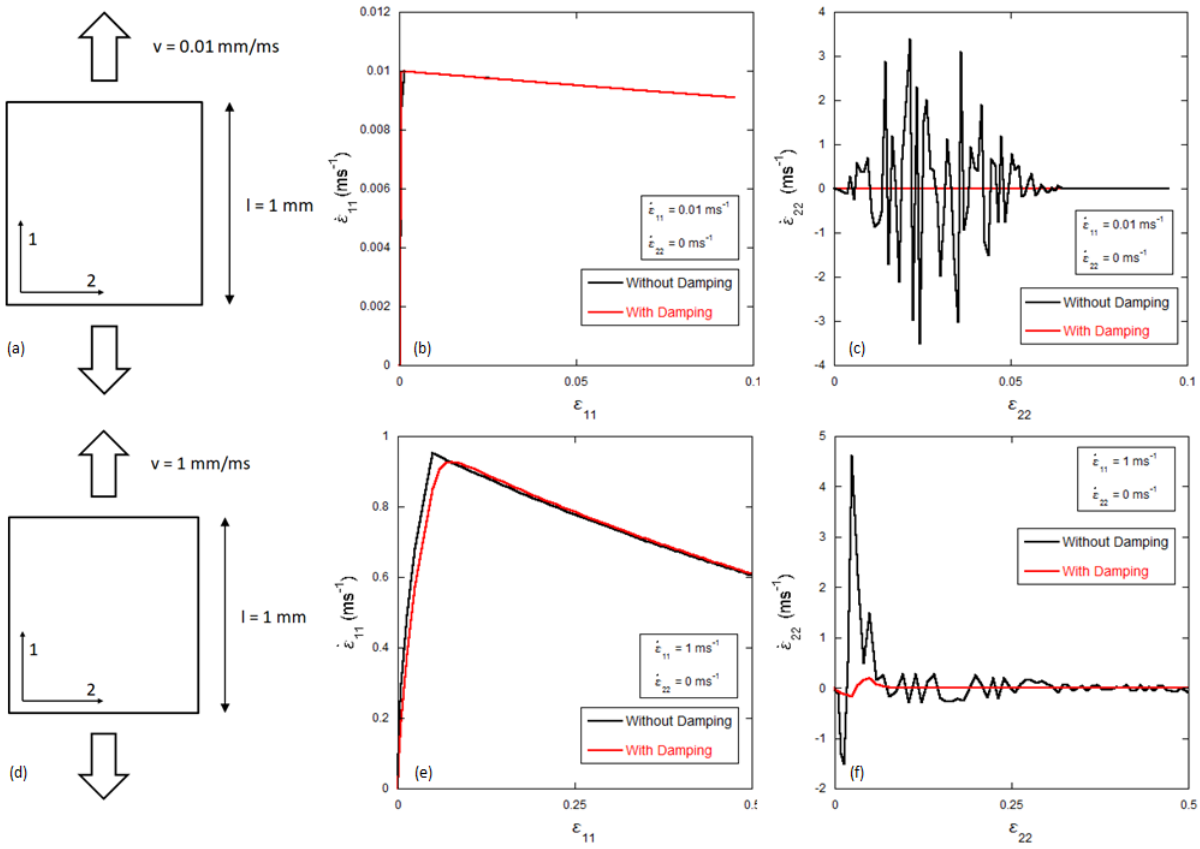

Figure 10: Performance of the damping algorithm with a damping coefficient $\xi = 0.999$ for medium and high strain rates along the principal direction (1) and comparison with the numerical value without damping $\xi = 0$. (a) Boundary conditions for medium strain rate loading, (b) strain rate vs strain along direction (1) and (c) strain rate vs strain along direction (2). (d) Boundary conditions for high strain rate loading, (e) strain rate vs strain along direction (1) and (f) strain rate vs strain along direction (2). Very high noise is appreciated in the numerical strain rate ($\xi = 0$) along the stress free direction (2).

4.2. Interlaminar damage model

Delamination between layers is replicated by means of a classical cohesive zone method using cohesive elements whose behavior is dictated by a traction-separation law [67]. A stress based damage initiation is considered following a quadratic interaction criteria between normal and shear stresses on the interface

$$\left(\frac{<t_n>}{N}\right)^2 + \left(\frac{t_s}{S}\right)^2 + \left(\frac{t_t}{S}\right)^2 = 1 \tag{38}$$

where t_n, t_s and t_t are the normal and shear elastic stresses acting on the interface and N and S stand for the normal and shear interface strengths, respectively. The Macaulay operator included in the normal tractions ensure that a purely compressive displacement or a purely compressive stress state does not initiate damage. Once the stress failure criterion is fulfilled, the damage evolves depending on the interply toughness Γ_C of the interface according to

the Benzeggah-Kenane (BK) fracture criterion [10], that accounts for the dependence of the fracture energy dissipation on the mode mixity:

$$\Gamma_C = \Gamma_{Ic} + (\Gamma_{IIc} - \Gamma_{Ic}) \left(\frac{\Gamma_s + \Gamma_t}{\Gamma_n + \Gamma_s + \Gamma_t} \right)^{\eta} \tag{39}$$

where Γ_{Ic}, Γ_{IIc} are the critical energy release rates for delamination in modes I and II respectively, assuming $\Gamma_{IIc} = \Gamma_{IIIc}$. Γ_n, Γ_s, Γ_t are the work done by the tractions and their conjugate relative displacements in the normal and shear directions and η corresponds to the Benzeggagh-Kenane parameter and determines the increase in toughness with the amount of mode mixity [63].

5. Low velocity impact tests

The numerical model was validated by means of low velocity impact tests. Experimental results were available in the literature for the glass fibre composite and are described in this section for the shake of completion [60]. Composite panels were manufactured by hot pressing. Curing was carried out at 1.8 bars of pressure in two consecutive steps at 130 and 180 °C at temperature rate of 2 °C/min. The laminates had 18 plies with stacking sequence $[(\pm\ 45/0/90)_2/0]_S$, 4.9 mm thickness and 8.2 kg/m^2 areal weight.

Low velocity impact tests were carried out using an Instron Dynatup 8250 drop weight testing machine. Square specimens of 145 x 145 mm^2 were cut from the composite panels and plates were simply supported by the fixture and hold at the corners with special clamping tweezers, leading to a free impact area of 127 x 127 mm^2. The specimens were impacted at the center using a 12.7 mm diameter steel tup. Incident impact energies of 42 and 94 J were chosen by selecting the weight and the height of the tup was adjusted to obtain an impact velocity of $\approx$ 4 m/s. The impact was instrumented with a 50 kN load cell and an accelerometer to record continuously the applied force and the tup displacement. Damage on the composite plates was ascertained by means of ultrasound. C-scans were performed on a TecniTests instrument. The backside (non-impacted) surface of the plates was scanned at 30 mm/s using a Sonatest SLG 5-102 transducer of 10 mm in diameter with a center frequency of 5 MHz. The interval between levels was 1dB and the resolution was 1 mm. The commercial software Visual Scan V-1.0 was used to visualise the results.

The experimental force *vs* displacement curves presented consistent results and the scatter was very limited. The mechanical response was initially smooth and the impact energy was spent mostly in the elastic deformation of the plate. High frequency oscillations in the load were observed in all curves prior to the maximum load. They were caused by the brittle fracture of the fibres in tension at the backside surface of the plate as a result of bending. After fibre fracture, the load carried by the plate decreased with the penetration depth. Damage on the panels was localised around the impact point in the form of a narrow ring with asymmetrical delaminated patches.

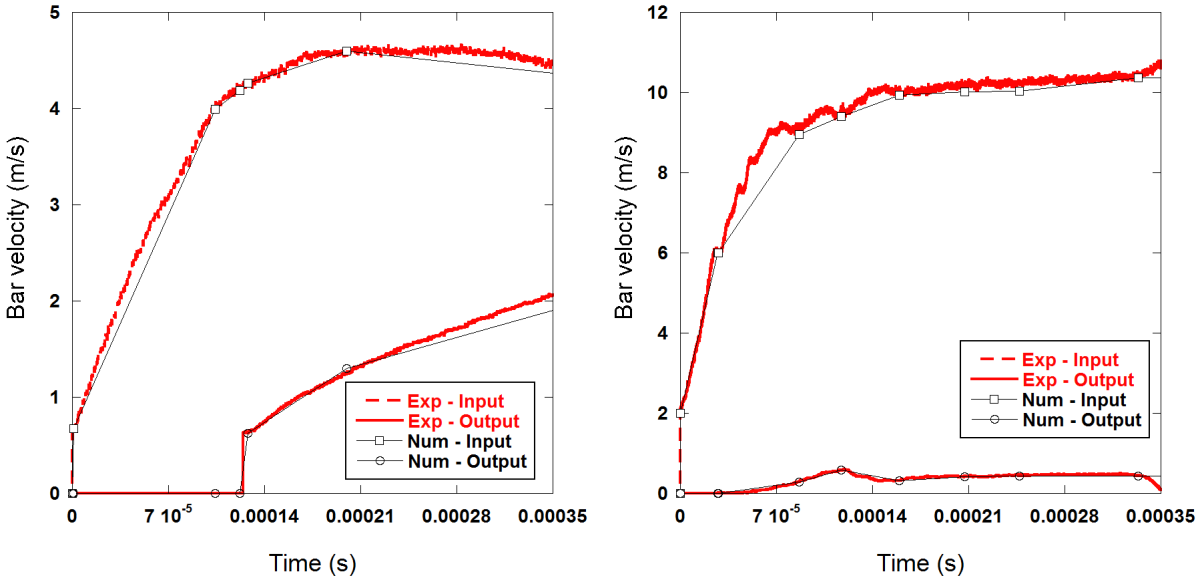

Figure 11: Boundary conditions for dynamic tests. Experimental and numerical input and output bar velocities for (a) tensile tests and (b) shear tests.

6. Numerical implementation

The constitutive model developed in the previous section has been implemented as a VUMAT subroutine in Abaqus/Explicit. The explicit integration scheme was adequate to compute the internal variables of the proposed model, which required very small strain increments to ensure stability. The model was structured in three different steps to account for the updated strain rate. For every single time step, it initially calculated the numerical strain rate (equation 37) and the equivalent strain rate considering the damping coefficient (equation 36). Afterwards it computed the rate dependent material properties (equation 35) and updated the stiffness matrix (equation 5), the yielding function for the non-linear shear response and the damage activation functions of each failure mode. These calculations were used to compute the damage variables, update the stiffness matrix and finally, provide the stresses. Material properties stop their evolution with the strain rate once the damage variables d_M got activated to ensure the correct energy dissipation.

The constitutive model was used to simulate the quasi-static and dynamic tests shown in previous section. To this end, each ply was discretised with 8 nodes reduced integration linear solid elements (C3D8R) with enhanced hourglass and distortion controls. Specimen geometries are shown in Figs.1(a) and (b) for tensile and shear tests respectively. Quasi-static tests were simulated clamping one of the edges of the specimens and imposing a low velocity of 0.01 m/s to the opposite boundary. Energy balance was evaluated to ensure inertia effects were negligible. Dynamic simulations were carried out enforcing the input and output bar velocities in the specimen ends as measured during the experiment, see Fig. 11 (a) for tensile and (b) for shear tests. This methodology was previously validated in dynamic characterisation of titanium alloys, reducing the computational costs of the simulations

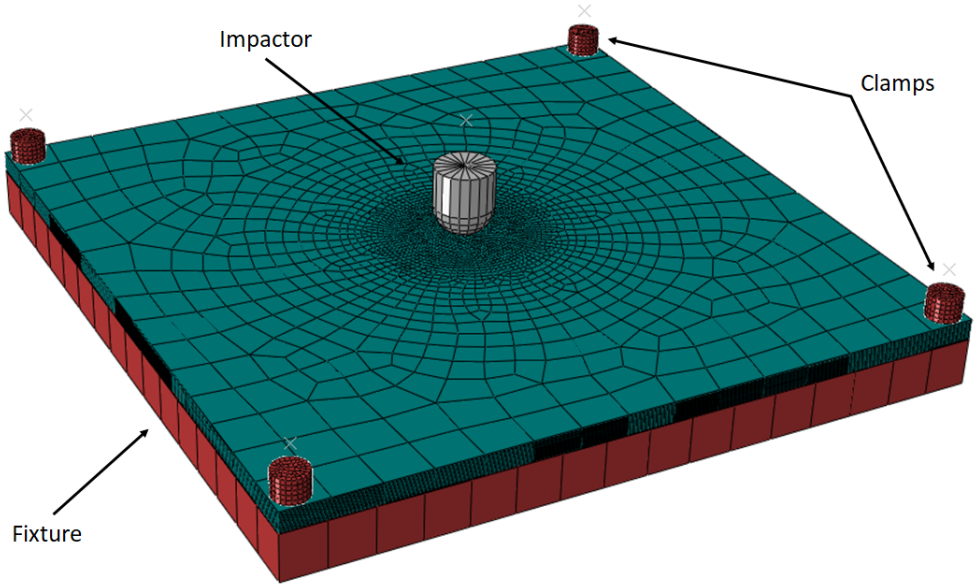

Figure 12: Finite element model to simulate drop weight tower impact tests. Clamps, fixture and impactor are considered solid bodies and the composite laminate includes the constitutive model and the cohesive elements to simulate the damage of the panel.

compared to the simulation of the whole Split-Hopkinson bar system [18]. It should be noted that the default bulk viscosity option in Abaqus was used in the simulations to eliminate instabilities in the numerical model at the onset of damage. To avoid high element distortion, an average damage variable D was defined for each Gauss point and elements with negligible internal energy ($D > 0.999$) were deleted from the simulation. Parametrical study of the damping coefficient to compute the numerical strain rate was accomplished. Dynamic tests with $\xi = 0$ aborted on the first time steps of the simulation and increasing the damping enhanced progressively the stability of the simulation. Finally, a damping coefficient of $\xi = 0.1$ was used for the numerical tests. In addition, mesh dependency was analysed for different characteristics lengths (2, 1 and 0.5 mm), showing similar results and demonstrating the objectivity of the numerical implementation, see AppendixA.

The developed constitutive model was used to simulate the drop weight tower tests reported in [60] for quasi-isotropic laminates manufactured on the same glass fibre composite. Geometry and boundary conditions are recalled in this section for the shake of completion. The laminates had 18 plies with stacking sequence $[(\pm\, 45/0/90)_2/0]_S$, 4.9 mm thickness and 8.2 kg/m^2 areal weight. Composite panels of 145 x 145 mm^2 were simply supported by the fixture and held at the corners with clamping tweezers, leading to a free impact area of 127 x 127 mm^2. The specimens were impacted at the centre using a 12.7 mm diameter steel tup at velocities of $\approx$ 4 m/s. Incident impact energies of 42 and 94 J were chosen to obtain different levels of damage.

The implementation of the numerical model follows the methodology presented in [58, 25], see Fig.12. The fixture and the clamps were discretised with rigid solid elements in contact

with the panel and the clamps applied a pressure of 0.25 GPa to the specimen. Pressure was introduced as an instantaneous distributed load, ensuring no damage was induced in the panel. The impactor was modelled as a rigid analytical surface associated with a lumped mass equal to 5.25 and 11.75 kg with initial drop velocity of 4 m/s resulting in the previous impact energies. The composite laminate was discretised at ply level with 8 nodes reduced integration linear solid elements (C3D8R) inserting three-dimensional cohesive elements (COH3D8) with 8.75μm thickness between plies to account for delamination. To avoid the mesh dependency inherent of crack propagation, central region of the laminate was refined with 1 mm size randomly oriented elements with no preferential alignment direction.

Contact between the impactor, the laminate, the fixture and the clamps was modelled using the general contact algorithm in Abaqus/Explicit, which uses a penalty enforcement contact method. This contact formulation was also applied between the different composite layers after the fully damaged cohesive elements were removed from the model. Friction was introduced between all the contacting surfaces with a friction coefficient $\mu = 0.3$. As before, damping coefficient was set to $\xi = 0.1$, enhanced hourglass and section controls were applied together with the default bulk viscosity and, in addition, the minimum time step in the numerical simulation was fixed to $\Delta t = 10^{-6}$ ms, ensuring the increment of mass due to mass scaling was never higher than the 2% of the total mass of the system.

7. Results and discussion

7.1. Material parameters

The constitutive model presented above relies in a number of parameters that determine the behaviour of the woven composite at ply level. Tensile and shear parameters for quasi-static and dynamic deformation regime were characterised in the previous section. Compressive strength, $X_C = Y_C$, was available in Matweb data base [46]. Out-of-plane characterisation of the material is not available in the literature, however, it is possible to find the mechanical properties of the MTM44-1 resin [53] which are a good approximation to the real out-of-plane Young Modulus of the composite, E_3. As an approximation, out-of-plane shear modulus and Poissons's ratios were assumed to have similar value as in-plane properties, $G_{12} = G_{31} = G_{23}$ and $\nu_{12} = \nu_{31} = \nu_{23}$. Intralaminar fracture toughnesses were not available in the literature neither, therefore, a sensitivity study was accomplished to analyse the influence of this parameter on the global response of the impacted target, see AppendixB. Shear fracture toughness, $\mathit{\Gamma}_{12}$, has been chosen as conservative as possible to avoid numerical snap-back. Finally the strain rate coefficients κ_T and κ_S for tensile and shear strengths were obtained considering the constraint imposed by equation 35 and the experimental data as detailed in Tables 1 and 2. Dependency of tensile and shear strengths as implemented in the constitutive model are plotted in Fig. 13. The yield shear strength coefficient κ_S^Y was fitted against the experimental curve as no data for high strain rates was available for low shear strains. A summary of all the material parameters in the model can be found in Table 3.

Table 3: 2D S-2 Glass Fibre/Epoxy Mechanical Properties

Physical properties (kg/m^3)	
Density (ρ)	1722
Quasi-static elastic properties (GPa)	
Young Moduli ($E_1 = E_2$)	22.66
Out-of-plane Young Modulus (E_3) [53]	4
Poisson's Coefficients ($\nu_{12} = \nu_{31} = \nu_{23}$)	0.375
In-plane Shear Modulus (G_{12})	4.3
Out-of-plane Shear Modulus ($G_{31} = G_{23}$)	4.3
Quasi-static strengths (GPa)	
Tensile strength ($X_t = Y_t$)	0.49
Compressive strength ($X_c = Y_c$) [46]	0.59
In-plane shear strength (S_{12})	0.13
In-plane shear yield (S_{12}^{yield})	0.043
Quasi-static fracture toughness (N/mm)	
Tensile fracture toughness ($\Gamma_{1+} = \Gamma_{2+}$)	80
Compressive fracture toughness ($\Gamma_{1-} = \Gamma_{2-}$)	40
In-plane shear fracture toughness (Γ_{12})	5
Strain rate coefficients (ms)	
Tensile strength coefficient (κ_T)	0.94
Ultimate Shear strength coefficient (κ_S)	0.07
Yield Shear strength coefficient (κ_S^Y)	2.0
Failure strains	
In-plane shear failure strain ($\gamma_{12}^{failure}$)	0.13

Interply properties were assumed to be controlled by the matrix and independent of the orientation of the adjacent plies. This approach sets the strength of the interface at the same level of the strength of the resin and can be considered and upper bound of the interface resistance. Normal interface strength N was employed as well to define the damage envelope of the matrix cracking failure mode, equation 25. Properties were obtained from the literature [49] and can be found in Table 4.

7.2. Tensile and shear response

The tensile and shear responses of the woven composite were simulated and compared with the previous experimental results at coupon level. The numerical and experimental nominal stress (force per cross section) *vs* the engineering strain is plotted in Fig.14 for tensile and Fig.15 for shear tests at quasi-static and dynamic loading regimes. The numerical results in these figures were obtained with a mesh discretization including 0.5 mm length finite elements. Simulations were carried out with different mesh sizes (in the range 0.25 to 1 mm) are shown in AppendixA and presented equivalent results. Dynamic simulations were carried out with a damping coefficient $\xi = 0.1$ and instabilities did not appear during

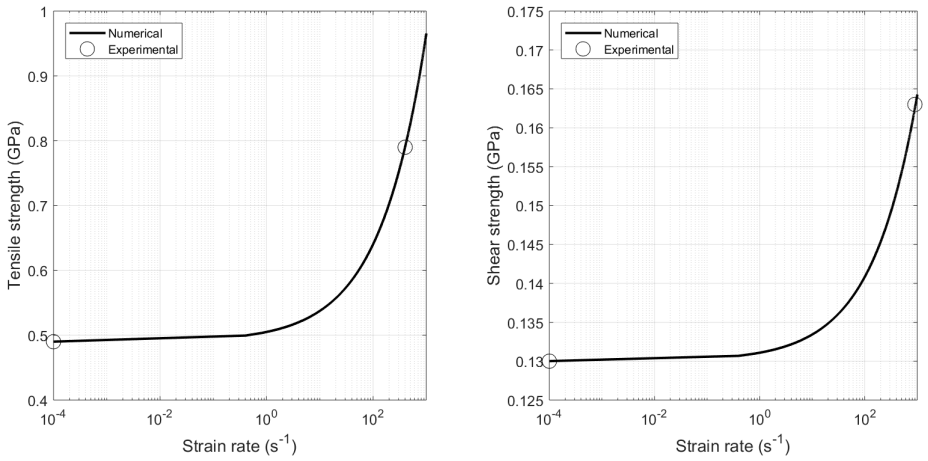

Figure 13: Rate dependent parameters as implemented in the constitutive model. (a) Tensile strength and (b) Shear strength.

Table 4: Interply properties [49]

Normal interface strength, N (MPa)	53
Shear interface strength, S (MPa)	104
Mode I fracture toughness, Γ_{Ic}(N/mm)	0.3
Mode II fracture toughness, Γ_{IIc}(N/mm)	0.8
Benzeggagh-Kenane parameter, η	1.75

the simulations. Numerical and experimental results were in very good agreement. Rate dependent tensile linear and shear non-linear responses were accurately predicted. However, the main difference was identified in the peak strength of tensile specimens as a result of the induced triaxial stress, predicting the damage localisation for lower applied forces. Triaxiality had major influence in dynamic regime due to the higher stresses. Better accuracy was obtained for shear tests, as crack localisation appeared exactly at the centre of the specimen, however, final strain to failure was overestimated as a consequence of the complex crack pattern. Hence, the constitutive model was able to provide strain rate dependent mechanical responses of the material while ensuring the stability of the numerical simulations.

The accuracy of the model was also checked by comparing the numerical and experimental results of the distribution of the logarithmic strain over the specimen, obtained in the experiments by means of digital image correlation. They are depicted in Figs.16 and Figs.17 for tensile and shear response, respectively. The numerical simulations captured the homogeneous deformation of the specimens in both configurations before the onset of damage (3.4% of deformation for tensile tests and 13% of deformation for shear tests) as well as the damage localisation for both failure modes. The constitutive model predicted the stress concentration produced at the edge of the gauge length in the tensile specimens due to the triaxial stress state created by the change in curvature, generating a single crack

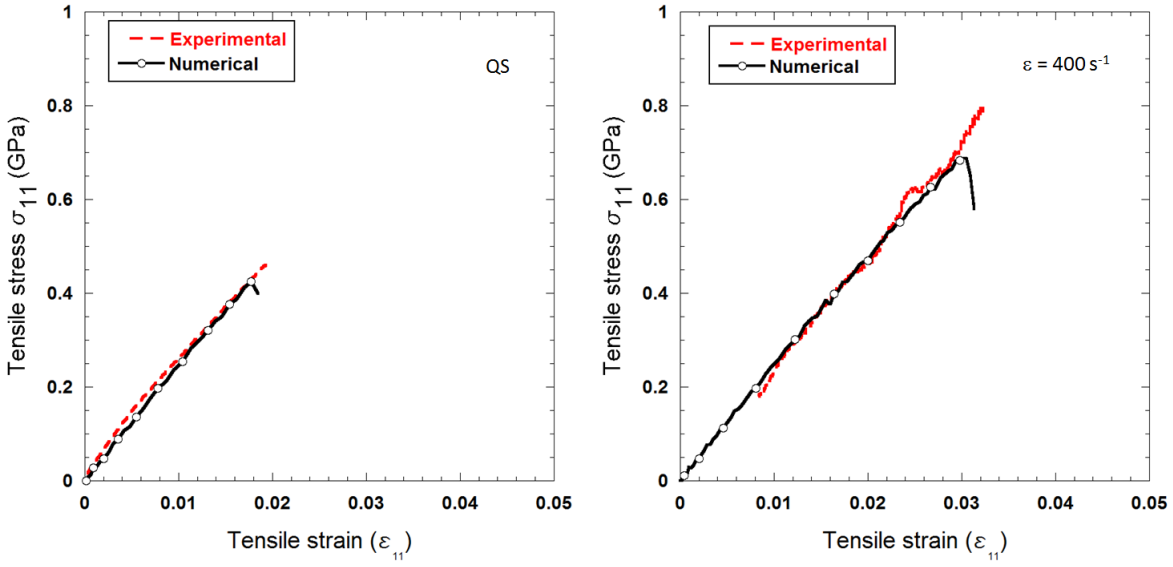

Figure 14: Nominal stress *vs.* engineering strain curves for specimens subjected to tensile load. (a) Quasi-static and (b) dynamic regime at 400 s^{-1}. The solid lines correspond to the numerical simulations while the broken lines stand for the experimental results.

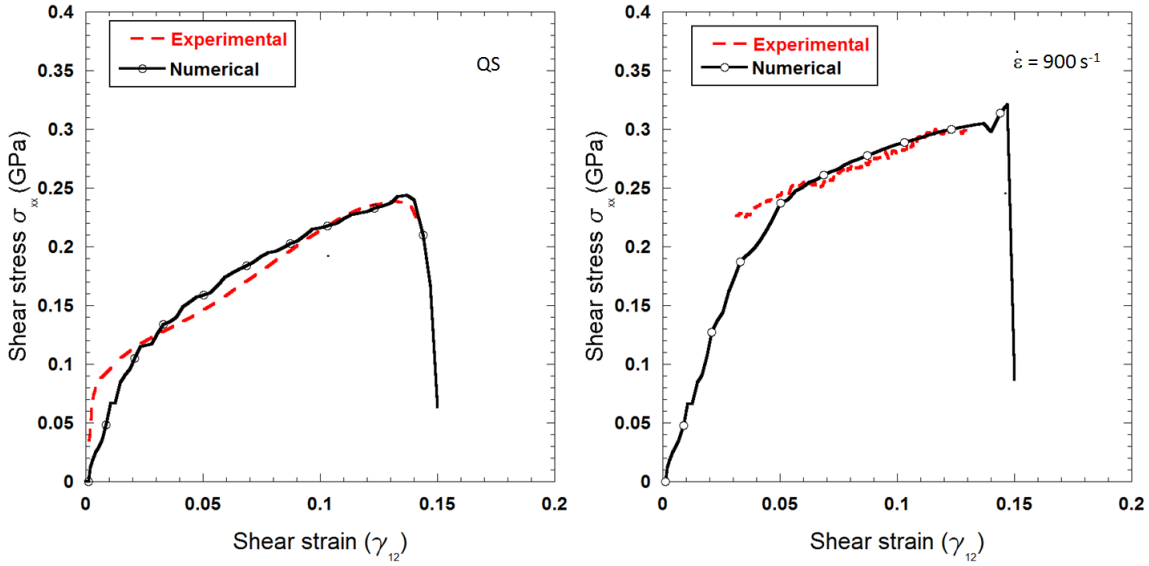

Figure 15: Nominal stress *vs.* engineering strain curves for specimens subjected to shear load. (a) Quasi-static and (b) dynamic regime at 900 s^{-1}. σ_{xx} stands for the stress measured in the global coordinate system, as included in equation 1. The solid lines correspond to the numerical simulations while the broken lines stand for the experimental results.

along that section. The model also predicted the damage localisation for shear failure at the central region of the gauge length with cracks oriented at 45° following the fibre direction.

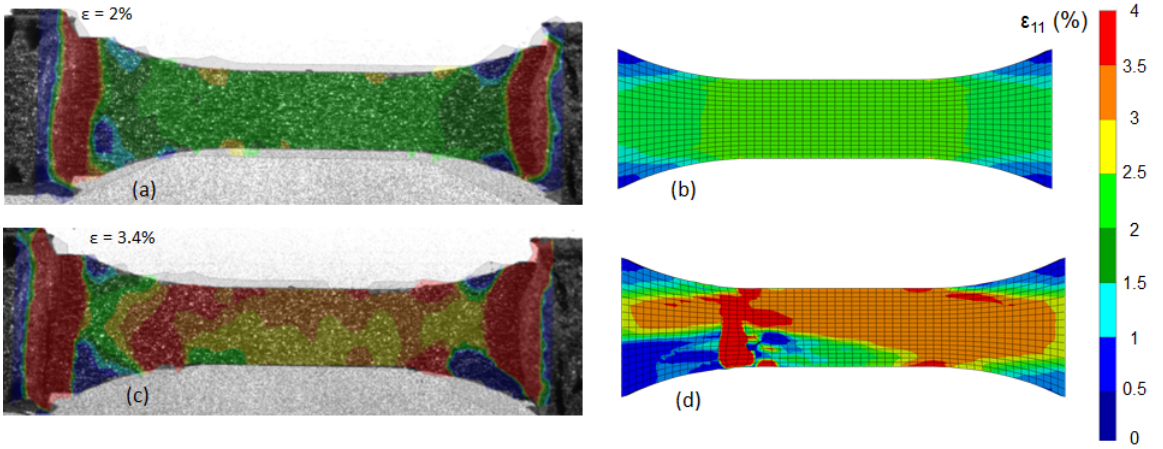

Figure 16: Experimental (a, c) and numerical (b, d) contour plots of the logarithmic tensile strain ε_1 at different values of applied strain. (a) and (b) 2%. (c) and (d) 3.25%.

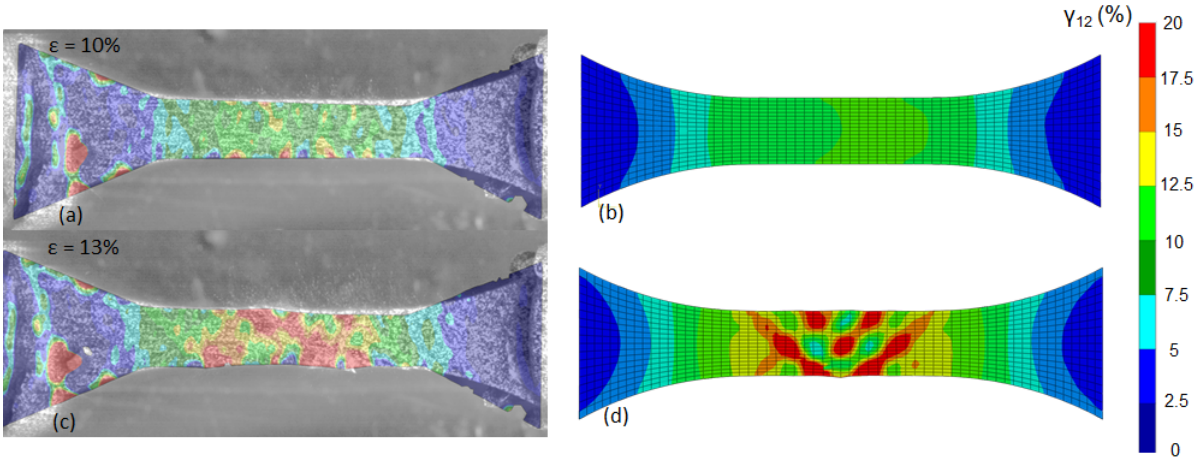

Figure 17: Experimental (a, c) and numerical (b, d) contour plots of the logarithmic shear strain γ_{12} at different values of applied strain. (a) and (b) 10%. (c) and (d) 14%.

7.3. Drop weight tower tests

After validation, the constitutive model was used to predict the low velocity impact response of the woven composite. The load *vs.* displacement curves, for experimental and numerical results are shown in Fig.18 for (a) 42 and (b) 94 J of impact energy. No numerical instabilities appeared during the simulation when setting the damping parameter at $\xi = 0.1$. The curve trends between experiments and the rate dependent simulations correlated reasonable well. The plate stiffness and the maximum impact force were captured by the model. Main difference appeared after the peak load for the high energy impact, see Fig.18(b), overestimating the maximum impactor deflection and permanent indentation. This variance can be attributed to the used of a 2D failure criteria that did not take into account relevant dissipation mechanisms for high energy impacts such as through-the-thickness

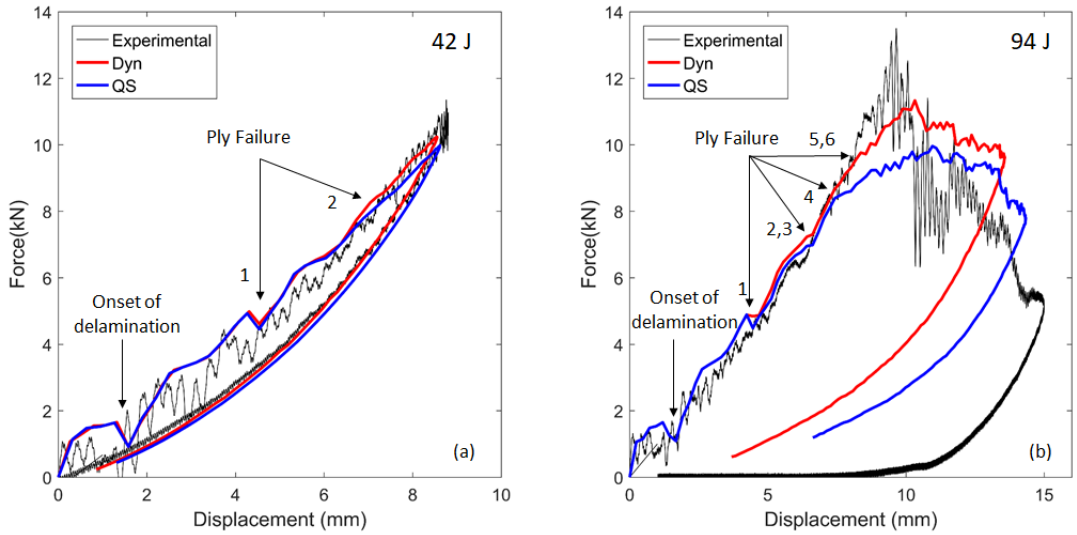

Figure 18: Comparison between experimental and numerical load-deflection curves for impact energies (a) 42 J and (b) 94 J. Simulations were carried out under strain rate dependent (Dyn) and independent (QS) cases. Ply failure sequence for the rate dependent hypothesis has been included.

shear and crushing [2]. The use of a 2D constitutive model virtually decreased the energy dissipated by the target during impact, leading to the discrepancies between the numerical and exponential unloading curves.

The performance of the strain rate dependent formulation (Dyn) was compared against the baseline constitutive model under strain rate-independent hypothesis (QS). Negligible difference was appreciated for the low velocity energy impact, see Fig.18(a), as the Young's moduli of the material and the delamination criteria were defined strain rate independent. Nevertheless, the strain-rate dependent model obtained a better prediction of the maximum impact force for the high energy impact, see Fig.18(b). At this energy level, fibre breakage and matrix cracking dominated the mechanical response of the composite, hence, the dynamic tensile and shear strength of the material played an important role on the overall resistance of the laminate. The rate-independent formulation overestimated the impact force, leading to a premature failure of the composite. Fracture toughness was defined as strain rate independent, therefore, similar energy dissipations were obtained for both hypothesis after the peak load.

The numerical simulations also provided insight on the strain rates and the wave propagation phenomena during impact. Contour plots of the strain rates for 94 J of impact energy are plotted in Fig.19 before and after onset of damage and softening localisation. During the first stages of the impact, see Fig.19(a), tensile strain rates of the order of 30 s^{-1} appeared at the rear face of the impacted laminate. The medium strain rate led to a ply strength increment, which explained the difference in failure sequence between the rate-dependent and independent constitutive models, as appreciated in the load-displacement curves, see Fig.18(b). As the impact force increased and matrix cracking was initiated, strain-softening

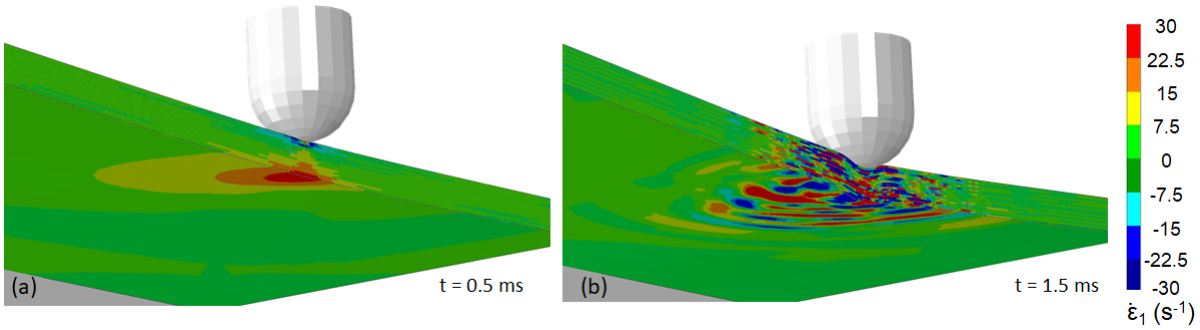

Figure 19: Contour plots of the strain rate for impact energy of 94 J. (a) t = 0.5 ms, before onset of damage and (b) t = 1.5 ms, after onset of damage.

regions were developed. The damaged elements emitted unloading strain waves, resulting in an unrealistic stress propagation. Numerically, the difference in stiffness matrices creates micro-impedances between elements, leading to an uncontrolled wave transmission, see Fig.19(b). This behaviour is an actual limitation of the continuum damage mechanics framework, that accounts for microstructural defects phenomenologically and can not predict the real physics of the heterogeneous damaged media [6, 12].

The numerical model also provided detail of the complex failure sequence during impact. Fibre damage on the panels at maximum deflection of the impactor is shown in Fig.20 and Fig. 21 for (a) 42 and (b) 94 J of impact energy, respectively. For the low impact energy level, barely visible impact damage was obtained. Delamination occurred at an approximate load of 1.5 kN and was concentrated around the impact point. Further loading triggered the matrix cracking and yarn failure modes on the first rear layer, at just about 5 kN force. Afterwards, cracks propagated along the through-the-thickness direction, reaching the second rear layer at a force of 8 kN. Maximum impact force was registered for 10 kN and the damaged area was restrained under the impactor. All these events resulted in a drop in the applied force by the impactor and a softening of the stiffness of the plate, captured by the numerical load-displacement curves, in reasonable agreement with the experimental results, see Fig.18(a). Increasing the impact energy heavily increased the damage suffered by the laminate. As the impact force raised, further cracks developed along in-plane direction in a cross-shaped pattern parallel to the yarn orientation, see Fig.21 (b). At approximately 12 kN of impact force, the crack propagation became unstable and the maximum load capacity of the laminate was attained, see Fig.18(b).

The performance of the model was also compared in terms of delamination. The numerical prediction for 42 J impact energy was correlated against the C-Scan of the post-mortem specimen [60]. Good correlation was obtained in terms of delamination extension for the low energy impact, see Fig.22(a). Delamination was localised around the impact point in the form of a narrow ring with asymmetrical delaminated patches. Larger delamination appeared at the rear plies of the laminate due to the bending of the plate. C-Scan for 94 J impact energy was not available, however, simulation showed a higher delamination area still restraint in the central region of the laminate, see Fig.22(b). In this case, higher energy

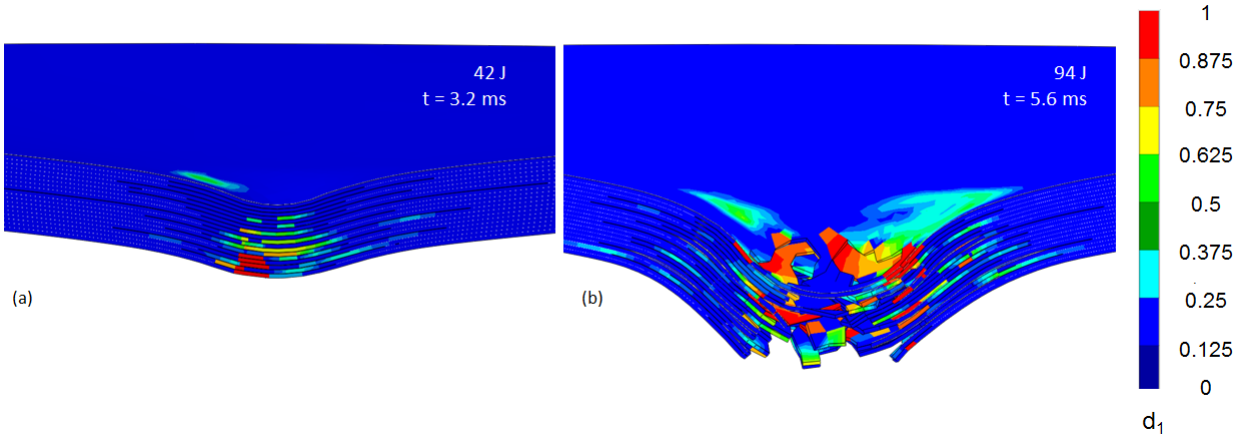

Figure 20: Damage along the through-the-thickness direction at maximum deflection of the tup. Contour plots of the damage variable d_1. (a) 42 J of impact energy at t = 3.2 ms and (b) 94 J of impact energy at t = 5.6 ms.

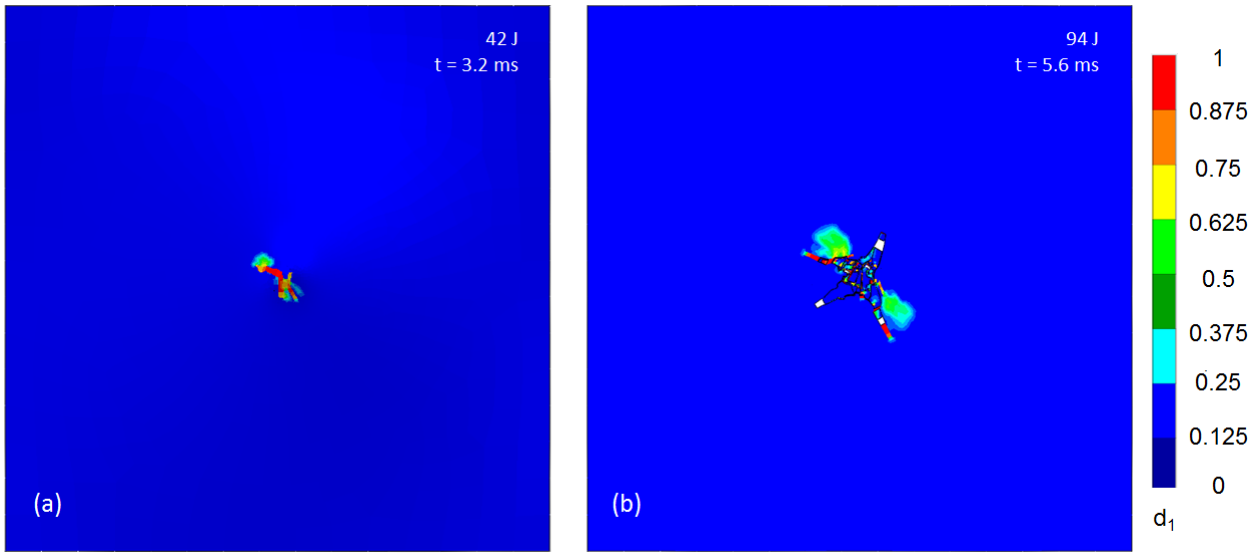

Figure 21: Damage on the rear face of the laminate at maximum deflection of the tup. Contour plots of the damage variable d_1. (a) 42 J of impact energy at t = 3.2 ms and (b) 94 J of impact energy at t = 5.6 ms.

failure modes were triggered and, therefore, delamination became a secondary dissipation mechanisms.

8. Conclusions

A stable strain rate dependent constitutive model for woven composites was developed and the low velocity impact response of a glass woven composite laminate was study from the experimental and simulation viewpoints. Tensile and shear tests were accomplished at

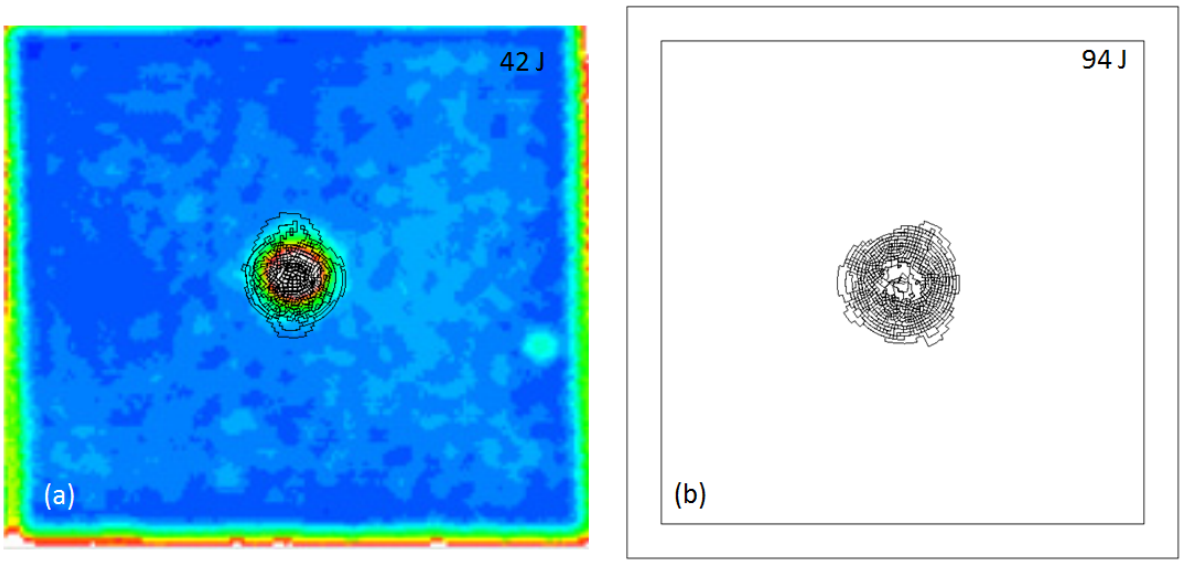

Figure 22: (a) Correlation between experimental and numerical delaminations for an impact energy of 42 J. Numerical delamination is superimposed over the C-scans for comparison purposes [60]. (b) Delamination predicted for impact energy of 94 J.

quasi-static and dynamic regimes to determine the material properties, the failure mechanisms and the strain rate dependency. Non standard split-Hopkinson bar specially design for composites was employed to ensure dynamic force equilibrium. Deformation was monitored be means of high-speed 2D DIC and main failure modes for quasi-static and dynamic conditions were characterised. Tensile response of the material was driven by the strength of the glass fibres while shear response was dominated by the epoxy resin and failure was caused by the progressive cracking of the matrix and yarn pull-out. Highest strain rate dependency was provided by the glass fibres, presenting a remarkable 160% increment of the tensile strength for 400 s^{-1} strain rate. Moderate strain rate dependency was also characterised for the shear response with a 130% strength increment for 900 s^{-1}.

The physical findings were used to develop a constitutive model able to account for strain rate effects. The model was intended to be used within the framework of the explicit finite element method and provided the constitutive response of the composite at ply level. A continuum damage mechanics approach was used to account for yarn breakage and matrix cracking failure modes and evolution of damage was implemented by a phenomenological softening function controlled by the fracture toughness of the material at each particular direction. The shear response accounted for the accumulated damage due to matrix cracking and a new formulation of the non linear shear behaviour suitable for explicit integration schemes was proposed. The formulation presented good convergence for small time steps and avoided the use of time consuming non linear systems of equations. Strain rate dependency was implemented in the ply properties together with a damping algorithm for stability purposes.

The model was validated at coupon level and provided strain rate dependent mechanical

responses of the material while ensuring the stability of the numerical simulations. The results of the finite element simulations of the tensile and shear tests were in very good agreement with the experimental data in terms of the nominal stress-strain curves and the strain fields. The model also captured the different failure modes and the crack generation and propagation after the onset of damage. Finally, the constitutive model was used to simulate the low velocity impact response of composite plates subjected to different impact energies. Reasonably good correlations were obtained in terms of maximum impact force, stiffness of the panel and failure of the composite. Delamination patterns were correctly predicted as well. The numerical model showed the wave propagation phenomena and the strain rates, predicting the appearance of instant tensile strain rates in the rear plies of the laminate of the order of 30 s^{-1}. The medium strain rates induced a moderate increment of the strength of the layers, which delayed the failure of the plies and increased the maximum impact force. In general, the rate-independent model overestimated the maximum impact force, and therefore, these results showed that strain rate dependency should be taken into account to accurately predict the low velocity impact response of glass-fibre laminates. Moreover, this research establishes the basis for the development of 3D strain rate dependent failure criteria to simulate the ballistic response of composite panels, where strain rates of around 100-500 s^{-1} are expected. This will be the topic of a forthcoming publication.

9. Acknowledgment

This research was supported by the Startup funding for recently appointed Lecturers of the University of Edinburgh. The collaboration of Dr. C. González, Ms. V. Martínez and Dr. R. Seltzer (IMDEA Materials Institute) to manufacture the panels and provide the data of the low velocity impact tests is gratefully acknowledged. In addition, we thank the assistance of Mr. J. Fullerton and Mr. S. Carter to manufacture the specimens and the help of Dr. A. Pellegrino (University of Oxford) to carry out the dynamic tests. The feedback and corrections of Dr. N. Bombace are kindly acknowledged. The authors would finally like to acknowledge Rolls-Royce plc, for their continuous support through the Solid Mechanics University Technology Centre at the University of Oxford.

AppendixA. Mesh objectivity

The mesh regularisation approach implemented through the softening parameters A_M was validated using different element discretisations to ensure energy dissipation was independent on the refinement. Three initial element sizes (0.25, 0.5 and 1 mm) were used and the corresponding nominal stress-strain curves are depicted in Figs. A.23 and A.24 for tensile and shear responses respectively, together with the contour plot of the damage variables at the onset of localisation. The differences in terms of the nominal stress-strain curves were very small and the damage patterns were also equivalent, predicting a similar crack propagation. Coarser meshes presented higher difficulties to capture the crack path particularly for shear tests, although they predicted the damage pattern phenomenologically. On

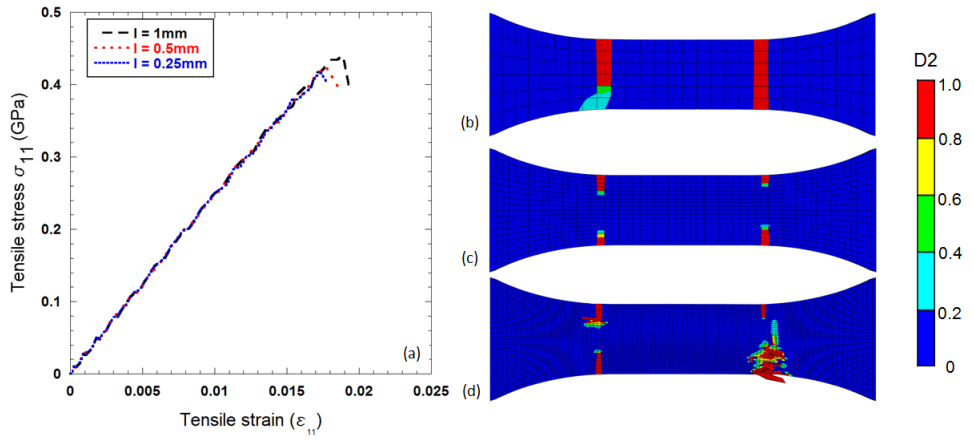

Figure A.23: Effect of the element size on the numerical tensile response. (a) Nominal stress *vs.* engineering strain curves for different element sizes. Contour plot of the damage variable d_2 at the onset of damage (approximately 2% of deformation) with (b) l $\approx$ 1 mm, (c) l $\approx$ 0.5 mm and (d) l $\approx$ 0.25mm.

the other hand, finer meshes were more prone to give numerical problems due to excessive element distortion after the onset of damage. It should be noticed that the computational cost of the simulations increased when decreasing the element size due to the larger number of elements and the reduction in the time step.

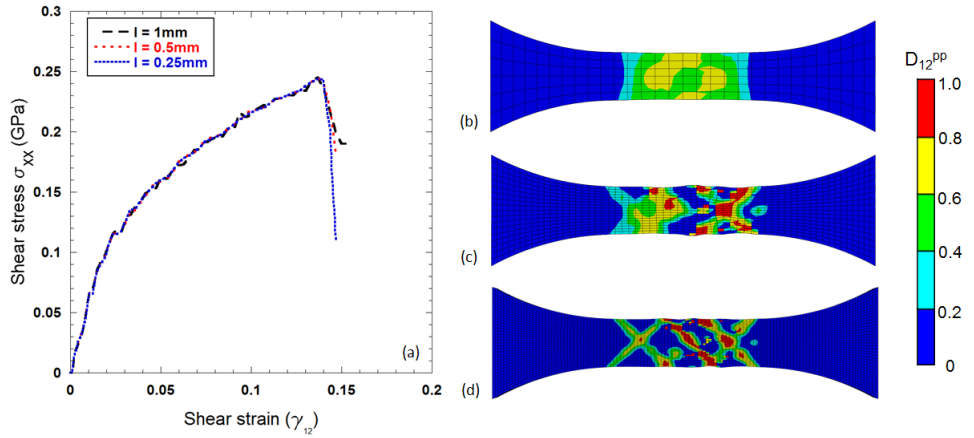

Figure A.24: Effect of the element size on the numerical shear response. (a) Nominal stress *vs.* engineering strain curves for different element sizes. Contour plot of the damage variable d_{12}^{pp} at the onset of damage (approximately 13% of deformation) with (b) l $\approx$ 1 mm, (c) l $\approx$ 0.5 mm and (d) l $\approx$ 0.25mm.

AppendixB. Fracture toughness: parametrical study

A parametrical study of the influence of the fracture toughness for tensile failure of the yarns (Γ_{1+} and Γ_{2+}) was carried out to understand the dependency on the stiffness of the panel when subjected to low velocity impact. The dynamic characterisation of the fracture

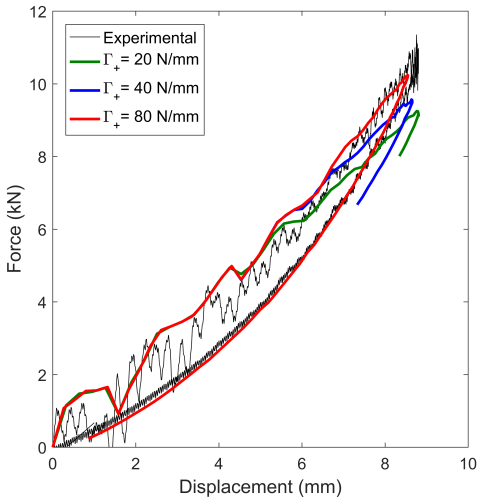

Figure B.25: Parametrical study of the influence of the fracture toughness Γ_{1+} and Γ_{2+} on the force-displacement curve of the woven composite when subjected to 42 impact energy.

toughness of composite materials requires the use of novel experimental techniques still under development and, to the authors knowledge, only available in few research laboratories [43], therefore, the proposed methodology tries to circumvent the issue, providing a reasonable numerical tool, carefully validated at coupon level. Baseline parameters for glass fibre composite were taken from [22, 39]. Fig. B.25 shows the correlation between the experimental load-displacement curve for an impact energy of 42 J, and the numerical results obtained for 3 different sets of material properties. The energy release rate associated to tensile damage of the yarns played an important role on the failure of the rear plies. Increasing the fracture toughness delayed the crack propagation, resulting in a higher stiffness of the plate, thus, increasing the maximum impact load and decreasing the maximum deflection of the laminate. Very good correlation was obtained for a value of $\Gamma_{1+} = \Gamma_{2+} = 80$ N/mm, which was used along the present publication.

AppendixC. Bibliography

[1] Akil, Ö., Yildirim, U., Güden, M., Hall, I. W., 2003. Effect of strain rate on the compression behaviour of a woven fabric S2-glass fiber reinforced vinyl ester composite. Polymer Testing 22 (8), 883–887.

[2] Alonso, L., Navarro, C., García-Castillo, S. K., 2018. Analytical models for the perforation of thick and thin thickness woven-laminates subjected to high-velocity impact. Composites Part B: Engineering 143, 292–300.

[3] Arao, Y., Taniguchi, N., Nishiwaki, T., Hirayama, N., Kawada, H., 2012. Strain-rate dependence of the tensile strength of glass fibers. Journal of Materials Science 47 (12), 4895–4903.

[4] ASTM, 2007. Standard Test Method for In-Plane Shear Response of Polymer Matrix Composite Materials by Tensile Test of a 45 Laminate. Vol. 94.

[5] Bai, X., Bessa, M. A., Melro, A. R., Camanho, P. P., Guo, L., Liu, W. K., 2015. High-fidelity micro-scale modeling of the thermo-visco-plastic behavior of carbon fiber polymer matrix composites. Composite Structures 134, 132–141.

[6] Bazant, B. Z. P., Belytschko, T. B., Chang, T.-P., 1985. Continuum theory for strain-softening. Journal of Engineering Mechanics 110 (12), 1666–1692.
[7] Bažant, Z. P., 1978. Spurious reflection of elastic waves in nonuniform finite element grids. Computer Methods in Applied Mechanics and Engineering 16 (1), 91–100.
[8] Bazant, Z. P., Planas, J., 1997. Fracture and size effect in concrete and other quasibrittle materials. CRC Press.
[9] Belingardi, G., Mehdipour, H., Mangino, E., Martorana, B., 2016. Progressive damage analysis of a rate-dependent hybrid composite beam. Composite Structures 154, 433–442.
[10] Benzeggagh, M. L., Kenane, M., Aldcb, A., 1996. Measurement of mixed-mode delamination fracture toughness of unidirectional glass/epoxy composites with mixed-mode bending apparatus. Composites Science and Technology 56 (96), 439–449.
[11] Berthe, J., Brieu, M., Deletombe, E., 2013. Improved viscoelastic model for laminate composite under static and dynamic loadings. Journal of Composite Materials 47 (14), 1717–1727.
[12] Bombace, N., 2018. Multi-scale simulation of dynamic phenomena in solid mechanics. Ph.D. thesis, University of Oxford.
[13] Bouvet, C., Castanié, B., Bizeul, M., Barrau, J. J., 2009. Low velocity impact modelling in laminate composite panels with discrete interface elements. International Journal of Solids and Structures 46 (14-15), 2809–2821.
[14] Buitrago, B. L., Santiuste, C., Sánchez-Sáez, S., Barbero, E., Navarro, C., 2010. Modelling of composite sandwich structures with honeycomb core subjected to high-velocity impact. Composite Structures 92 (9), 2090–2096.
[15] Chen, J. F., Morozov, E. V., 2016. A consistency elasto-viscoplastic damage model for progressive failure analysis of composite laminates subjected to various strain rate loadings. Composite Structures 148, 224–235.
[16] Cousigné, O., Moncayo, D., Coutellier, D., Camanho, P., Naceur, H., 2014. Numerical modeling of non-linearity, plasticity and damage in CFRP-woven composites for crash simulations. Composite Structures 115 (1), 75–88.
[17] Cousigné, O., Moncayo, D., Coutellier, D., Camanho, P., Naceur, H., Hampel, S., 2013. Development of a new nonlinear numerical material model for woven composite materials accounting for permanent deformation and damage. Composite Structures 106, 601–614.
[18] Cousins, B., 2016. Development of improved numercal techniques for high strain rate deformation behaviour of Titanium alloys. Ph.D. thesis, University of Oxford.
[19] Cui, H., Thomson, D., Pellegrino, A., Wiegand, J., Petrinic, N., 2016. Effect of strain rate and fibre rotation on the in-plane shear response of 45 laminates in tension and compression tests. Composites Science and Technology 135, 106–115.
[20] Daggumati, S., De Baere, I., Van Paepegem, W., Degrieck, Xu, J., Lomov, S. V., Verpoest, I., 2010. Local damage in a 5-harness satin weave composite under static tension: Part I - Experimental analysis. Composites Science and Technology 70, 1926–1933.
[21] Daniel, I. M., Werner, B. T., Fenner, J. S., 2011. Strain-rate-dependent failure criteria for composites. Composites Science and Technology 71 (3), 357–364.
[22] Donadon, M. V., Falzon, B. G., Iannucci, L., Hodgkinson, J. M., 2007. Intralaminar toughness characterisation of unbalanced hybrid plain weave laminates. Composites Part A: Applied Science and Manufacturing 38 (6), 1597–1611.
[23] Donadon, M. V., Iannucci, L., Falzon, B. G., Hodgkinson, J. M., de Almeida, S. F. M., 2008. A progressive failure model for composite laminates subjected to low velocity impact damage. Computers and Structures 86 (11-12), 1232–1252.
[24] English, S. A., Briggs, T. M., Nelson, S. M., 2016. Quantitative validation of carbon-fiber laminate low velocity impact simulations. Composite Structures 135, 250–261.
[25] Garijo, D., Martínez-Hergueta, F., Lopes, C. S., Llorca, J., González, C., Puente, J. L., Loya, J. A., Toral-Vázquez, J., Votsios, V., Martino, E., 2018. Multiscale FE Modelling and Design of Composite Laminates Under Impact. In: Comprehensive Composite Materials II. Vol. 8. pp. 219–238.

[26] Gerlach, R., Kettenbeil, C., Petrinic, N., 2012. A new split Hopkinson tensile bar design. International Journal of Impact Engineering 50, 63–67.
[27] Gigliotti, L., Pinho, S. T., 2015. Multiple length/time-scale simulation of localized damage in composite structures using a Mesh Superposition Technique. Composite Structures 121, 395–405.
[28] Gillespie, J. W., Gama, B. A., Cichanowski, C. E., Xiao, J. R., 2005. Interlaminar shear strength of plain weave S2-glass/SC79 composites subjected to out-of-plane high strain rate compressive loadings. Composites Science and Technology 65 (11-12), 1891–1908.
[29] Goldberg, R., Roberts, G., 2008. Approximation of nonlinear unloading effects in the strain rate dependent deformation analysis of polymer matrix materials utilizing a state variable approach. Journal of Aerospace Engineering 21 (July), 119–131.
[30] Goldberg, R. K., Roberts, G. D., Gilat, A., 2005. Implementation of an Associative Flow Rule Including Hydrostatic Stress Effects into the High Strain Rate Deformation Analysis of Polymer Matrix Composites. Journal of Aerospace Engineering 18 (1), 18–27.
[31] GOM-Correlate, 2015. GOM Correlate Professional, Inspection and Testing. GOM mbH.
[32] Hashin, Z., 1980. Failure Criteria for Unidirectional Fibre Composites. Journal of Applied Mechanics 47 (June), 329–334.
[33] Hochard, C., Aubourg, P. A., Charles, J. P., 2001. Modelling of the mechanical behaviour of woven-fabric CFRP laminates up to failure. Composites Science and Technology 61 (2), 221–230.
[34] Hufner, D. R., Hill, S. I., 2017. High strain rate testing and modeling of a woven E-glassvinylester composite in dry and saturated conditions. Journal of Composite Materials 51 (21), 3017–3039.
[35] Iannucci, L., 2006. Progressive failure modelling of woven carbon composite under impact. International Journal of Impact Engineering 32 (6), 1013–1043.
[36] Ishikawa, T., Chou, T., 1982. Stiffness and strength behaviour of woven fabric composites. Journal of Materials Science 17 (11), 3211–3220.
[37] Kerschbaum, M., Hopmann, C., 2016. A Progressive Damage Model for unidirectional Fibre Reinforced Composites with Application to Impact and Penetration Simulation. Applied Composite Materials 23 (3), 495–522.
[38] Khan, A. S., Colak, O. U., Centala, P., 2002. Compressive failure strengths and modes of woven S2-glass reinforced polyester due to quasi-static and dynamic loading. International Journal of Plasticity 18 (10), 1337–1357.
[39] Kinvi-Dossou, G., Matadi Boumbimba, R., Bonfoh, N., Koutsawa, Y., Eccli, D., Gerard, P., 2018. A numerical homogenization of E-glass/acrylic woven composite laminates: Application to low velocity impact. Composite Structures 200 (May), 540–554.
[40] Koerber, H., Xavier, J., Camanho, P. P., 2010. High strain rate characterisation of unidirectional carbon-epoxy IM7-8552 in transverse compression and in-plane shear using digital image correlation. Mechanics of Materials 42 (11), 1004–1019.
[41] Kolsky, H., 1949. An investigation of the mechanical properties of materials at very high rates of loading. Proceedings of the Physical Society B 62 (11), 676.
[42] Lemaitre, J., 1996. A course on damage mechanics. Springer-Verlag Berlin Heidelberg.
[43] Liu, H., Nie, H., Zhang, C., Li, Y., 2018. Loading rate dependency of Mode I interlaminar fracture toughness for unidirectional composite laminates. Composites Science and Technology 167 (April), 215–223.
[44] Llorca, J., González, C., Molina-Aldareguía, J. M., Segurado, J., Seltzer, R., Sket, F., Rodríguez, M., Sádaba, S., Muñoz, R., Canal, L. P., 2011. Multiscale modeling of composite materials: A roadmap towards virtual testing. Advanced Materials 23 (44), 5130–5147.
[45] Martinez-Hergueta, F., 2016. Multiscale analysis of the mechanical behaviour of needle-punched non-woven fabrics. Ph.D. thesis, Technical University of Madrid.
[46] MatWeb-LLC, 2018. MatWeb Data Base. http://www.matweb.com/.
[47] May, M., 2015. Numerical evaluation of cohesive zone models for modeling impact induced delamination in composite materials. Composite Structures 133, 16–21.
[48] Mouritz, A. P., Gellert, E., Burchill, P., Challis, K., 2001. Review of advanced composite structures for

naval ships and submarines. Composite Structures 53 (1), 21–24.
[49] Muñoz, R., Martínez-Hergueta, F., Gálvez, F., González, C., LLorca, J., 2015. Ballistic performance of hybrid 3D woven composites: Experiments and simulations. Composite Structures 127, 141–151.
[50] Naik, N. K., Ganesh, V. K., 1995. An analytical method for plain weave fabric composites. Composites 26 (4), 281–289.
[51] Naik, N. K., Yernamma, P., Thoram, N. M., Gadipatri, R., Kavala, V. R., 2010. High strain rate tensile behavior of woven fabric E-glass/epoxy composite. Polymer Testing 29 (1), 14–22.
[52] Navarro, P., Aubry, J., Marguet, S., Ferrero, J. F., Lemaire, S., Rauch, P., 2012. Semi-continuous approach for the modeling of thin woven composite panels applied to oblique impacts on helicopter blades. Composites Part A: Applied Science and Manufacturing 43 (6), 871–879.
[53] Naya, F., Molina-Aldareguía, J. M., Lopes, C. S., González, C., Llorca, J., 2017. Interface Characterization in Fiber-Reinforced PolymerMatrix Composites. Jom 69 (1), 13–21.
[54] Qiao, P., Yang, M., Bobaru, F., 2008. Impact Mechanics and High-Energy Absorbing Materials : Review. Journal of Aerospace Engineering 21 (October), 235–248.
[55] Raimondo, L., Iannucci, L., Robinson, P., Curtis, P. T., 2012. Modelling of strain rate effects on matrix dominated elastic and failure properties of unidirectional fibre-reinforced polymer-matrix composites. Composites Science and Technology 72 (7), 819–827.
[56] Richardson, M., Wisheart, M., 1996. Review of low-velocity impact properties of composite materials. Composites Part A: Applied Science and Manufacturing 27 (12), 1123–1131.
[57] Richeton, J., Schlatter, G., Vecchio, K. S., Rémond, Y., Ahzi, S., 2005. A unified model for stiffness modulus of amorphous polymers across transition temperatures and strain rates. Polymer 46 (19 SPEC. ISS.), 8194–8201.
[58] Sádaba, S., Martínez-Hergueta, F., Lopes, C., Gonzalez, C., J. LLorca, 2015. Virtual testing of impact in fiber reinforced laminates. In: Structural Integrity and Durability of Advanced Composites. pp. 247–270.
[59] Schaefer, J. D., Werner, B. T., Daniel, I. M., 2018. Progressive Failure Analysis of Multi-Directional Composite Laminates Based on the Strain-Rate-Dependent Northwestern Failure Theory. Experimental Mechanics Series 58, 487–497.
[60] Seltzer, R., González, C., Muñoz, R., Llorca, J., Blanco-Varela, T., 2013. X-ray microtomography analysis of the damage micromechanisms in 3D woven composites under low-velocity impact. Composites Part A: Applied Science and Manufacturing 45, 49–60.
[61] Shi, Y., Swait, T., Soutis, C., 2012. Modelling damage evolution in composite laminates subjected to low velocity impact. Composite Structures 94 (9), 2902–2913.
[62] Suppakul, P., Bandyopadhyay, S., 2002. The effect of weave pattern on the mode-I interlaminar fracture energy of E-glass/vinyl ester composites. Composites Science and Technology 62 (5), 709–717.
[63] Systemes, D., 2010. Abaqus 6.10 User's manual.
[64] Tang, X., Whitcomb, J. D., 2003. Progressive Failure Behaviours of 2D Woven Composites. Journal of Composite Materials 37 (14), 1239–1259.
[65] Thiruppukuzhi, S. V., Sun, C. T., 2001. Models for the strain-rate-dependent behavior of polymer composites. Composites Science and Technology 61 (1), 1–12.
[66] Treutenaere, S., Lauro, F., Bennani, B., Haugou, G., Matsumoto, T., Mottola, E., 2017. Constitutive modelling of the strain-rate dependency of fabric reinforced polymers. International Journal of Impact Engineering 108, 361–369.
[67] Turon, A., Dávila, C. G., Camanho, P. P., Costa, J., 2007. An engineering solution for mesh size effects in the simulation of delamination using cohesive zone models. Engineering Fracture Mechanics 74 (10), 1665–1682.
[68] Van Paepegem, W., De Baere, I., Degrieck, J., 2006. Modelling the nonlinear shear stress-strain response of glass fibre-reinforced composites. Part I: Experimental results. Composites Science and Technology 66 (10), 1455–1464.
[69] Wang, K., Zhao, L., Hong, H., Zhang, J., 2018. A strain-rate-dependent damage model for evaluating the low velocity impact induced damage of composite laminates. Composite Structures, In press.

[70] Werner, B. T., Daniel, I. M., 2014. Characterization and modeling of polymeric matrix under multi-axial static and dynamic loading. Composites Science and Technology 102, 113–119.
[71] Wiegand, J., 2008. Constitutive modelling of composite materials under impact loading. Ph.D. thesis, University of Oxford.
[72] Xu, J., Lomov, S., Verpoest, I., Daggumati, S., Van Paepegem, W., Degrieck, J., 2015. A progressive damage model of textile composites on meso-scale using finite element method: Fatigue damage analysis. Computers & Structures 152, 96–112.